Synchrotron FTIR imaging of OH in quartz mylonites

Andreas K. Kronenberg[1], Hasnor F. B. Hasnan[1,a], Caleb W. Holyoke III[1,b], Richard D. Law[2], Zhenxian Liu[3], and Jay B. Thomas[4]

[1]Center for Tectonophysics, Department of Geology and Geophysics, MS 3115, Texas A&M University,
College Station, TX 77843-3115, USA
[2]Department of Geosciences, MC 0420, Derring Hall RM 4044, Virginia Polytechnic Institute and State University,
Blacksburg, VA 24061, USA
[3]Geophysical Laboratory, Carnegie Institution of Washington, 5251 Broad Branch Rd., NW Washington, D.C. 20015, USA
[4]Department of Earth Sciences, 204 Heroy Geology Laboratory, Syracuse University, Syracuse, NY 13244, USA
[a]now at: Department of Advanced Geophysics, PETRONAS, Carigali Sdn. Bhd., PETRONAS Twin Towers, Kuala Lumpur
City Centre, 50088 Kuala Lumpur, Malaysia
[b]now at: Department of Geosciences, University of Akron, Akron, OH 44325-4101, USA

Correspondence to: Andreas K. Kronenberg (kronenberg@geo.tamu.edu)

Abstract. Previous measurements of water in deformed quartzites using conventional Fourier transform infrared spectroscopy (FTIR) instruments have shown that water contents of larger grains vary from one grain to another. However, the non-equilibrium variations in water content between neighboring grains and within quartz grains cannot be interrogated further without greater measurement resolution, nor can water contents be measured in finely recrystallized grains without including absorption bands due to fluid inclusions, films, and secondary minerals at grain boundaries.

Synchrotron infrared (IR) radiation coupled to a FTIR spectrometer has allowed us to distinguish and measure OH bands due to fluid inclusions, hydrogen point defects, and secondary hydrous mineral inclusions through an aperture of $10\,\mu m$ for specimens $> 40\,\mu m$ thick. Doubly polished infrared (IR) plates can be prepared with thicknesses down to 4–$8\,\mu m$, but measurement of small OH bands is currently limited by strong interference fringes for samples $< 25\,\mu m$ thick, precluding measurements of water within individual, finely recrystallized grains. By translating specimens under the $10\,\mu m$ IR beam by steps of 10 to $50\,\mu m$, using a software-controlled $x - y$ stage, spectra have been collected over specimen areas of nearly $4.5\,mm^2$. This technique allowed us to separate and quantify broad OH bands due to fluid inclusions in quartz and OH bands due to micas and map their distributions in quartzites from the Moine Thrust (Scotland) and Main Central Thrust (Himalayas).

Mylonitic quartzites deformed under greenschist facies conditions in the footwall to the Moine Thrust (MT) exhibit a large and variable $3400\,cm^{-1}$ OH absorption band due to molecular water, and maps of water content corresponding to fluid inclusions show that inclusion densities correlate with deformation and recrystallization microstructures. Quartz grains of mylonitic orthogneisses and paragneisses deformed under amphibolite conditions in the hanging wall to the Main Central Thrust (MCT) exhibit smaller broad OH bands, and spectra are dominated by sharp bands at 3595 to $3379\,cm^{-1}$ due to hydrogen point defects that appear to have uniform, equilibrium concentrations in the driest samples. The broad OH band at $3400\,cm^{-1}$ in these rocks is much less common. The variable water concentrations of MT quartzites and lack of detectable water in highly sheared MCT mylonites challenge our understanding of quartz rheology. However, where water absorption bands can be detected and compared with deformation microstructures, OH concentration maps provide information on the histories of deformation and recovery, evidence for the introduction and loss of fluid inclusions, and water weakening processes.

1 Introduction

Quartz mylonites sheared at middle to lower levels of the continental crust exhibit microstructural and textural evidence of dislocation creep, a process that is widely believed to require water weakening in framework silicates. The effects of water on dislocation creep of quartz, including the nucleation, glide, climb and recovery of dislocations, and recrystallization are well known from (1) experimental studies of natural crystals, in which water was introduced into grain interiors (e.g., Griggs, 1967; Blacic, 1975, 1981; FitzGerald et al., 1991), (2) studies of synthetic and natural quartz varieties with large initial water contents (e.g., Griggs and Blacic, 1965; Hobbs, 1968; Baeta and Ashby, 1970; Kekulawala et al., 1978; Kirby and McCormick, 1979; McLaren et al., 1983; Linker et al., 1984; Gerretsen et al., 1989; Muto et al., 2011; Holyoke and Kronenberg, 2013; Stünitz et al., 2017), and (3) quartzites and polycrystalline quartz aggregates with water added or removed before or during experiments (e.g., Jaoul et al., 1984; Kronenberg and Tullis, 1984; Tullis and Yund, 1989; Hirth and Tullis, 1992; Gleason and Tullis, 1995; Post et al., 1996; Chernak et al., 2009). IR spectroscopy has played a key role in experimental studies of water weakening, through the characterization and measurement of OH absorption bands due to different hydrogen defects and forms of molecular water within quartz interiors (e.g., Kats, 1962; Griggs and Blacic, 1965; Aines and Rossman, 1984; Aines et al., 1984; Stipp et al., 2006).

Water weakening in the continental crust is inferred because of the high laboratory strengths exhibited by quartz and feldspars in the absence of water (Griggs, 1967; Heard and Carter, 1968; Tullis and Yund, 1977, 1980; Tullis, 1983; Blacic and Christie, 1984) and the postulated effects of water on point defects and disruptions of fully linked Si–O bonds (Griggs, 1974; Hirsch, 1979; Hobbs, 1981; Paterson, 1989). With the advent of FTIR and IR microscopes, water and hydrogen defects in naturally deformed quartz have been reported with OH contents of 300 to > 10 000 ppm (molar H/10^6Si; Kronenberg and Wolf, 1990; Kronenberg et al., 1990; Nakashima et al., 1995; Gleason and DeSisto, 2008; Seaman et al., 2013; Finch et al., 2016; Kilian et al., 2016), comparable to those required for water weakening in laboratory experiments. In small granitic shear zones deformed at greenschist conditions, water contents of quartz grains appear to correlate with finite strain (Kronenberg et al., 1990; Gleason and DeSisto, 2008), and in the much larger Median Tectonic Line of Japan, intragranular water contents increase towards its center (Nakashima et al., 1995). However, OH concentrations of quartz of granitic rocks deformed at higher temperatures can be much lower (20–100 ppm; Han et al., 2013; Kilian et al., 2016), with IR spectra dominated by small sharp OH bands of hydrogen point defects (Kilian et al., 2016) that are not thought to weaken quartz. Moreover, quartz water contents have been reported that show a trend of decreasing OH content towards the center of a high-grade

Table 1. Structural distances of samples below the Moine Thrust at the Stack of Glencoul (Law et al., 1986, 2010) and above the Main Central Thrust on the NW and Eastern Sutlej transects (Law et al., 2013). Deformation temperatures estimated by Law et al. (2013) using the Kruhl (1998) quartz *c*-axis fabric opening angle thermometer, and temperatures and pressures of metamorphism estimated by Stahr (2013) using THERMOCALC multi-equilibria thermometry (Powell and Holland, 1994) are indicated.

Moine Thrust – Stack of Glencoul mylonitic quartzites.			
Sample	Distance below MT		
SG-7	2.5 m		
SG-8	2.9 m		
SG-10	4.6 m		

Main Central Thrust – NW Sutlej transect orthogneisses			
Sample	Distance above MCT	T	
S09-30	~ 750 m	$\sim 600\,°C$[1]	
S09-35	75 m	$\sim 540\,°C$[1]	

Main Central Thrust – Eastern Sutlej transect paragneisses			
Sample	Distance above MCT	T	P
S09-58	~ 4500 m	735 °C[2]	900 MPa[2]
S09-63	~ 1500 m	675 °C[2]	850 MPa[2]
S09-71B	25 m	610 °C[1]	

[1] Deformation temperature estimated from quartz *c*-axis fabric opening angle (Law et al., 2013). [2] Temperature and pressure of metamorphism estimated from THERMOCALC multi-equilibra thermobarometry (Stahr, 2013, p. 67; Law et al., 2013).

shear zone (Finch et al., 2016). Maps of OH content, constructed from FTIR spectra of deformed granitic rocks (Seaman et al., 2013), show compelling relationships between water content and microstructures generated during deformation, suggesting that water contents are reduced during recrystallization and partial melting.

Much as deformation microstructures and textures provide a link between our understanding of deformation mechanisms activated in deformation experiments at high laboratory strain rates and the mechanisms governing plasticity and creep of shear zones at low natural strain rates (Snoke et al., 1998; Heilbronner and Barrett, 2014), IR spectroscopy can provide a link between our understanding of water weakening in the lab and in nature. In this paper, we report on methods of FTIR to characterize OH absorption bands and image OH contents in quartz (and other nominally anhydrous minerals) at higher resolution than is possible using conventional instruments, coupling synchrotron IR radiation with FTIR. We apply these methods to mylonitic quartzites in the footwall to the Moine Thrust in NW Scotland and to mylonitic quartz-rich orthogneisses and paragneisses in the hanging wall to the Main Central Thrust in NW India.

2 Selected quartz mylonites

The quartz mylonites selected to test synchrotron FTIR and imaging of OH come from the footwall of the Moine Thrust (MT) at the Stack of Glencoul, NW Scotland (Christie, 1963; Law et al., 1986, 2010), and the hanging wall of the Main Central Thrust (MCT) exposed in the Sutlej Valley, NW India (Law et al., 2013; Stahr, 2013; Law, 2014). Both of these thrust faults are orogen-scale shear zones with penetrative deformation on the MT accommodating shortening at the foreland edge of the Caledonian orogeny (e.g., Peach et al., 1907; Elliot and Johnson, 1980; Law et al., 1986, 2010; Butler, 2010; Law, 2010; Law and Johnson, 2010; Dewey et al., 2015) and penetrative shear strains on the MCT accommodating southward-directed Oligocene–Miocene extrusion/exhumation of the overlying Greater Himalayan slab (e.g., Grujic et al., 1996; Grasemann et al., 1999; Godin et al., 2006; Law et al., 2013). Mylonitic grain shape foliations are well developed in rocks of both fault zones and mineral stretching lineations are parallel to the fault transport directions. Deformation microstructures and textures of quartz in these mylonites indicate that dislocation creep was the predominant deformation mechanism involving both basal and prism slip systems, internal recovery, and dynamic recrystallization.

Structural distances of samples below the MT and above the MCT, together with available information on deformation temperatures and temperatures/pressures of metamorphism, are summarized in Table 1. All samples from the footwall to the MT are mylonitic Cambrian quartzites. Samples from the hanging wall to the MCT on the NW Sutlej transect are penetratively deformed orthogneisses in which intensities of grain shape fabrics, traced downwards towards the thrust surface, increase and dynamically recrystallized grain sizes decrease (Law et al., 2013; their Fig. 6). Samples from the more hinterland-positioned Eastern Sutlej transect are less obviously foliated paragneisses with more granular textures due to extreme quartz grain boundary mobility.

Mylonitic Cambrian quartzites in the footwall to the MT at the Stack of Glencoul (Assynt region) display highly flattened relict grains aligned parallel to foliation, with grain shape aspect ratios up to 50 : 1 to 100 : 1 and smooth undulatory extinction between crossed polarizers that have been described as quartz ribbons (Bonney, 1883; Christie, 1960, 1963; Weathers et al., 1979; Law et al., 1986). At the margins of the larger quartz grains, more equant, finely recrystallized grains overprint these elongate high-strain grains, with the proportion of new to old grains increasing structurally upwards towards the MT plane (Christie, 1960; Weathers et al., 1979; Law et al., 1986). Rare grains of feldspar and quartz aligned in "mechanically strong" orientations are relatively equant, and appear as augen or globular quartz grains. Quartz c axes exhibit strong lattice preferred orientations in both deformed old grains and recrystallized grains, with symmetrical type 1 (Lister, 1977) cross-girdle fabrics at distances

> 150 mm beneath the thrust plane and increasingly asymmetric cross-girdle to single girdle fabrics closer to the thrust plane (Law et al., 1986, 2010). These fabrics reflect general flattening strains accommodated by quartz basal and prism slip, with variations in estimated flow vorticities and partitioning of strain between original and recrystallized grains (Law et al., 2010; Law, 2010). Micas are highly aligned parallel to foliation, with coarse muscovite grains at quartz grain boundaries and fine, dispersed micas within quartz grain interiors. Optical microstructures show evidence of quartz recrystallization by bulge nucleation and subgrain rotation with relatively uniform mean recrystallized grain sizes of ∼ 15 µm (Christie et al., 1954; Weathers et al., 1979). Microstructures imaged by transmission electron microscopy (TEM) show dense arrays of curved free dislocations, subgrain walls, and fine fluid inclusions that decorate dislocations (Weathers et al., 1979; Ord and Christie, 1984). Earlier FTIR measurements of MT mylonites from a number of locations in the Assynt region revealed large OH absorption bands characteristic of milky quartz with OH contents of 1500 to 7500 ppm (Kronenberg and Wolf, 1990).

Quartz-rich Greater Himalayan Series orthogneisses and paragneisses in the hanging wall to the MCT exposed in NW and Eastern Sutlej transects, respectively, include quartz mylonites, quartz–mica schists, and quartz–garnet schists (Vannay and Grasemann, 1998; Grasemann et al., 1999; Law et al., 2013). Quartz grain shapes are not as highly elongate as observed in the MT mylonites, owing to their extensive recrystallization, with mean grain sizes on the NW transect that vary with structural level from 200 to 250 µm (grain boundary migration microstructures) at ∼ 1000 m above the MCT to 75–95 µm at 200–750 m above the thrust, and 35–60 µm (dominantly subgrain rotation microstructures) at ∼ 75 m above the thrust surface (Law et al., 2013). As noted above, quartz recrystallized grain sizes are much larger at a given structural height above the thrust plane on the hinterland-positioned eastern transect with grain sizes commonly ranging from 250 to > 1000 µm (0.25–1.0 mm) at ∼ 25 m above the thrust to > 1–2 mm at 200 m and higher above the thrust. Quartz grain interiors on the eastern transect display mild undulatory extinction with highly aligned subgrain boundaries that give the appearance of chessboard extinction and irregular, non-planar grain boundaries that envelope neighboring mica grains, suggestive of high grain boundary mobilities at the time of peak metamorphism and deformation. Quartz c axes show strong lattice preferred orientations with symmetrical and slightly asymmetrical cross-girdle fabrics on both transects, providing evidence of simultaneous basal and prism slip during plane strain deformation, with varying amounts of pure shear and simple shear (Law et al., 2013). Coarse-grained muscovite and biotite are highly aligned parallel to foliation, both at the boundaries of quartz grains and within quartz grain interiors.

While both the MT and the MCT mylonites were deformed by dislocation creep, their deformation tempera-

tures were very different and the mechanisms of recrystallization, accommodating dislocation creep differ accordingly. Deformation temperatures for the MT footwall mylonites at the Stack of Glencoul are estimated at between 300 and 350 °C based on illite crystallinity (Johnson et al., 1985). Opening angles of *c*-axis fabrics measured separately on old and recrystallized grains (Law et al., 2010) indicate far higher apparent deformation temperatures using the Kruhl (1998) fabric opening angle thermometer (390–440 and 475–530 °C, respectively) than are compatible with their prehnite-pumpellyite to lower greenschist (chlorite) facies phyllosilicates (Law, 2014). Deformation temperatures for MCT hanging wall mylonites range between ∼ 535 and 610 °C on the NW Sutlej transect, using the Kruhl (1998) opening angle thermometer, and ∼ 610–> 735 °C based on fabric opening angles and petrologic constraints on the Eastern Sutlej transect (Table 1; Law et al., 2013; Stahr, 2013).

Dynamic quartz recrystallization microstructures in the MT mylonites are similar to microstructures developed under experimental Regime II creep conditions as defined by Hirth and Tullis (1992), with a combination of bulge nucleation recrystallization (BLG) at grain boundaries and subgrain rotation recrystallization (SGR) within quartz grain interiors, and they are consistent with deformation under greenschist facies conditions (Stipp et al., 2002, 2010; Law, 2014). Quartz microstructures in the MCT mylonites (particularly on the Eastern Sutlej transect and at large distances above the thrust on the NW transect) indicate more internal recovery and more extensive grain boundary migration (GBM) than is apparent in the Regime III creep experiments of Hirth and Tullis (1992). The microstructures are more similar to those observed by Stipp et al. (2002, 2010) in quartz veins deformed at natural strain rates and the equivalent of middle–upper amphibolite facies conditions (∼ 550–700 °C; see review by Law, 2014).

The small recrystallized quartz grain sizes (16–9 μm), subgrain sizes, and dislocation densities of the MT footwall mylonites at the Stack of Glencoul imply large differential stresses (40–250 MPa) during shearing (Weathers et al., 1979; Ord and Christie, 1984); differential stresses of ∼ 55–85 MPa are recalculated using these grain sizes and the recrystallized grain size piezometer of Stipp et al. (2006; their Fig. 8) modified by the stress correction of Holyoke and Kronenberg (2010). In contrast, quartz recrystallized grain sizes for MCT mylonites on the NW Sutlej transect of 60–35 μm at 75 m above the thrust to 95–75 μm at 750–200 m above the thrust indicate lower differential stresses of 19–30 and 13–16 MPa, respectively, extrapolating the Stipp et al. (2006) grain size piezometer, adjusted by the same stress correction (Francsis, 2012; Law et al., 2013). Flow stresses inferred for the Eastern Sutlej transect mylonites would presumably be even lower than for mylonites of the NW Sutlej transect, but their grain sizes are far greater than those encompassed by any experimental grain size piezometer.

3 Methods

IR spectroscopy has been an important tool for studying OH defects in nominally anhydrous minerals and, in coordination with deformation experiments, to study the effects of water and hydrogen defects on mechanical properties (e.g., Kats, 1962; Griggs and Blacic, 1965; Kekulawala et al., 1978, 1981; Aines and Rossman, 1984; Cordier and Doukhan, 1991; Mackwell and Kohlstedt, 1991; Bai and Kohlstedt, 1996; Kohlstedt et al., 1996). With the introduction of efficient FTIR spectrometers and IR microscopes, studies of intragranular water and hydrogen defects in naturally deformed rocks have been enabled using apertures of 50–100 μm (Kronenberg and Wolf, 1990; Nakashima et al., 1995; Gleason and DeSisto, 2008; Finch et al., 2016; Kilian et al., 2016) as well as FTIR mapping of OH contents (Seaman et al., 2013). Molecular water contents of naturally deformed quartz commonly have large grain-to-grain variations at this scale of observation, and it has not been possible to measure OH contents of fine, dynamically recrystallized grains without including OH bands associated with grain boundaries.

Synchrotron-generated IR radiation is much brighter (∼ 1000×) than conventional globar sources of commercial FTIR instruments, and high-quality IR spectra can readily be measured through small (10 μm) apertures (Lobo et al., 1999; Carr et al., 2008; Ma et al., 2013). By coupling synchrotron radiation to a FTIR instrument and IR microscope, OH absorption bands can be measured through a 10 μm aperture with higher signal-to-noise ratio than through a 100 μm aperture using a standard FTIR system. We have measured OH concentrations using both conventional and synchrotron FTIR and we have mapped OH distributions using synchrotron FTIR within quartz grains and across multiple grains of MT and MCT mylonites.

3.1 Preparation of IR plates

Doubly polished IR plates of uniform thickness were prepared perpendicular to foliation and parallel to lineation for MT and MCT mylonites. Images of large IR plates were collected using a high-resolution (4000 dpi) Nikon slide scanner (Coolscan 8000 ED), with and without polarizing filters on both sides of the sample (Fig. 1a, b). Images of smaller IR plates were recorded with a Zeiss Axioplan 2 petrographic microscope and AxioCam HRc imaging system (Fig. 1c–f). Image contrast was enhanced digitally (using Adobe Photoshop) for crossed-polarized light images of ultrathin samples with small optical retardations. Throughout the preparation of IR plates, impregnation of samples by epoxy or other insoluble resins was avoided to prevent the introduction of OH or CH absorption bands of mounting media, which might be difficult to distinguish from OH bands of samples. While central regions of the IR plates remain fragile, metal frames were mounted to IR plate extremities for mechanical support, to avoid catastrophic loss and facilitate handling.
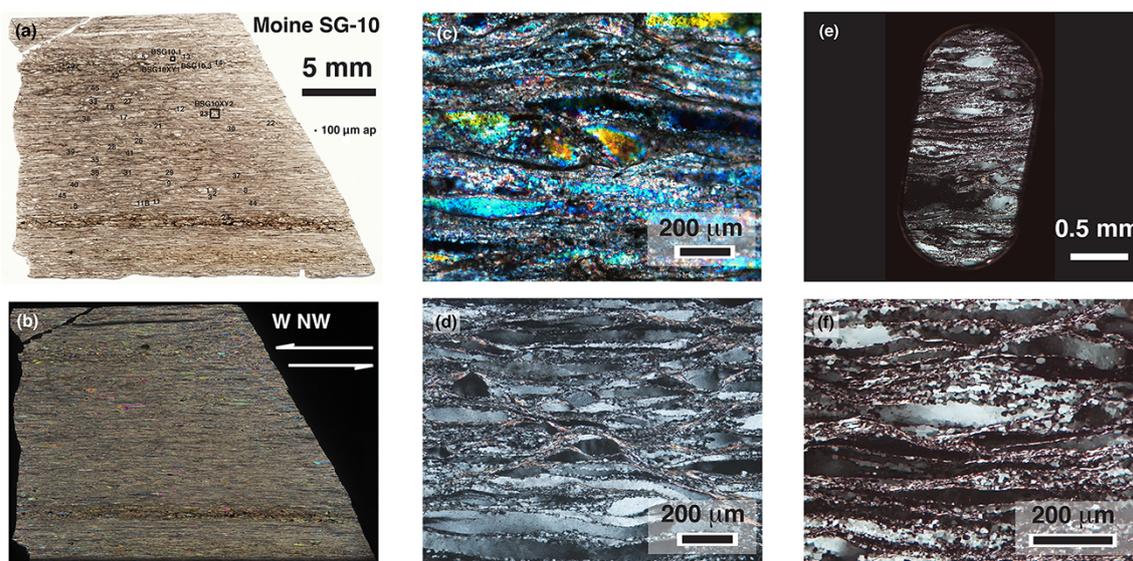
Figure 1. Doubly polished IR plates of Moine Thrust (MT) mylonites prepared perpendicular to foliation and parallel to lineation. **(a)** Low-magnification image of large IR plate prepared from Stack of Glencoul sample SG-10 (unpolarized light), with a mean thickness $t = 120\,\mu m$. **(b)** Same IR plate of SG-10 shown in **(a)** but with crossed-polarized light. The MT top to WNW shear sense is shown in the plane of the IR plate (top to the left). **(c)** Higher-magnification optical micrograph of large IR plate of sample SG-10, with crossed polarized light and local plate thickness ($117\,\mu m$) determined from IR interference fringes. **(d)** Optical micrograph of Stack of Glencoul sample SG-7 in crossed-polarized light (normal $30\,\mu m$ section thickness), illustrating deformation and recovery microstructures with higher resolution than in thick IR plates; note undulatory extinction in ribbon quartz grains, fine recrystallized grains, and aligned muscovite grains localized at quartz grain boundaries. **(e)** Low-magnification image of ultrathin IR plate of Stack of Glencoul sample SG-7-5 (crossed-polarized light) mounted on a copper TEM slot ring ($t = 4$–$8\,\mu m$, based on IR interference fringes). **(f)** Higher-magnification optical micrograph of the same IR plate SG-7-5 (crossed-polarized light) as shown in **(e)** with deformation and recrystallization microstructures shown more clearly than in normal $30\,\mu m$ thin section.

Oriented rock chips were first mounted on a glass thin section plate using CrystalBond 509 and a low-temperature hot plate. The top surfaces of samples were polished using a sequence of successively finer grits (400 and 600 mesh; 9.5, 3, and $0.3\,\mu m$). Polished specimens were removed from the glass plate and remounted, this time on their polished surfaces. Sample plates were cut parallel to the first surface, and the second (cut) surface was ground and polished to the desired thickness by the same method. A micrometer was used to measure the compound thickness of sample, glass plate, and mounting medium, checking thickness at sample extremities. In addition to micrometer measurements, sample thicknesses were tested during grinding, using interference colors for thicker samples (first-order colors for quartz plates 50–$90\,\mu m$ thick) and maximum detectable birefringence (grey–white scale) while polishing ultrathin ($< 20\,\mu m$) samples.

Before removing doubly polished samples from the glass thin section plate, metal frames were mounted to sample extremities using a thin bead of epoxy resin to provide support. For larger ($> 10\,mm$) samples with thicknesses of 25–$100\,\mu m$, metal frames made of Ni wire ($\sim 1\,mm$ diameter) were custom-fit to each sample. For thin samples ($< 25\,\mu m$), several metal frames normally used to mount TEM samples (3 mm outer diameter copper rings or slot rings with

$1 \times 2\,mm$ internal dimensions; supplied by Ted Pella, Inc., Fig. 1e) were mounted on each polished sample. Once the metal frames were attached and the epoxy cured, samples were removed from the glass thin section over a low-temperature hot plate, and the CrystalBond resin removed using acetone.

The fragile quartz IR plates, 4 to $150\,\mu m$ thick, were soaked in static acetone baths to dissolve the CrystalBond resin, exchanging the acetone and repeating this procedure three times. Even without ultrasonic agitation, some samples were damaged by air bubbles caught beneath them, leading to specimen warping and disintegration.

3.2 FTIR

IR absorption spectra were collected for quartz mylonites of varying plate thickness using a Nicolet Magna 560 FTIR instrument with Omnic software, a conventional globar source and NicPlan IR microscope (at Texas A&M University), and using a Bruker Hyperion FTIR instrument, OPUS software, and IR microscope at the U2A synchrotron beamline of the National Synchrotron Light Source (NSLS) I (at Brookhaven National Laboratory, Upton, NY). Both the Nicolet and Bruker instruments make use of liquid nitrogen-cooled MCT detectors. IR spectra were collected at a wavenumber reso-
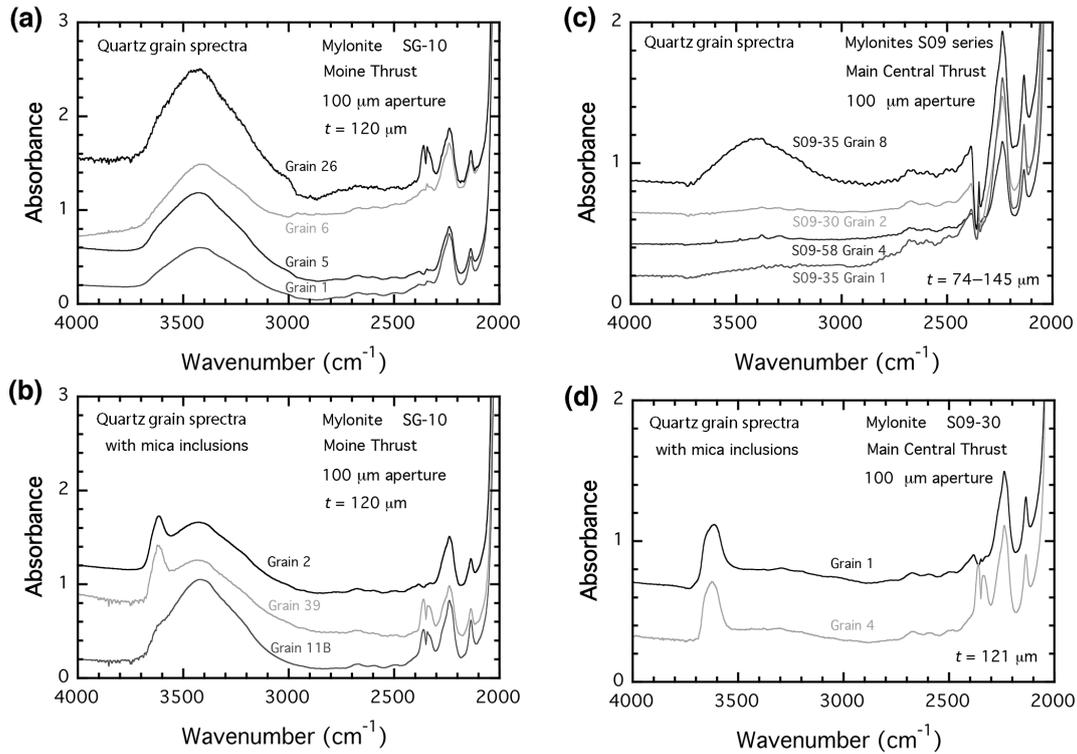
Figure 2. IR spectra of quartz grains in mylonites from the MT (Stack of Glencoul) and the Main Central Thrust (MCT, Sutlej Valley) using conventional FTIR with globar IR source through a 100 µm aperture. **(a)** Absorption spectra of quartz grains of MT IR plate SG-10 (shown in Fig. 1a–b) show a broad OH band at $3400\,\mathrm{cm^{-1}}$ due to fluid inclusions. **(b)** Absorption spectra of MT quartz grains of the same IR plate (SG-10) showing the same broad OH band and an OH absorption band (or shoulder) at $3600\,\mathrm{cm^{-1}}$ due to mica inclusions. **(c)** Absorption spectra of quartz grains of MCT IR plates S09-30 ($t = 121$ µm), S09-35 ($t = 74$ µm), and S09-58 ($t = 145$ µm), with many grains showing small sharp OH absorption bands due to hydrogen point defects, and less common grains with a large broad absorption band at $3400\,\mathrm{cm^{-1}}$. **(d)** Absorption spectra of quartz grains of MCT sample S09-30 ($t = 121$ µm) with a prominent OH band at $3600\,\mathrm{cm^{-1}}$ due to mica inclusions and smaller OH bands at lower wavenumbers. Absorbance values plotted vertically are normalized to represent their values for a uniform sample thickness of 1 mm.

lution of $4\,\mathrm{cm^{-1}}$, compiling 512 scans for each spectrum (or more if needed using the Nicolet FTIR), and spectra were stored over wavenumbers of 4000 to $2000\,\mathrm{cm^{-1}}$. For purposes of comparison, all absorbances shown in spectra for quartz grains of varying thickness have been normalized to a common thickness of 1 mm.

Representative IR spectra of individual quartz grains from MT and MCT samples measured with the Nicolet FTIR (100 µm aperture) exhibit OH absorption bands of variable size and character (Fig. 2). MT quartz spectra show a broad OH stretching band at $3400\,\mathrm{cm^{-1}}$ of large but variable magnitude (Fig. 2a), characteristic of molecular water in fluid inclusions of milky quartz (Kekulawala et al., 1978; Aines and Rossman, 1984; Stünitz et al., 2017). In addition to this absorption band, some quartz grains from MT samples show an additional absorption band (or subtle shoulder) at $\sim 3600\,\mathrm{cm^{-1}}$ (Fig. 2b) due to fine-scale micas (sometimes visible optically and sometimes too fine to resolve) dispersed within quartz grains. MCT quartz spectra tend to have smaller OH absorption bands (Fig. 2c), with some grains

showing small sharp bands at 3595, 3482, 3431, 3408, and $3379\,\mathrm{cm^{-1}}$ due to hydrogen interstitial defects (Kats, 1962; Aines and Rossman, 1984) and less common grains with a larger broad band at $3400\,\mathrm{cm^{-1}}$. Finely dispersed micas are less common in these coarser-grained mylonites, but some quartz grains also exhibit a $3600\,\mathrm{cm^{-1}}$ OH band due to micas (Fig. 2d).

Aside from differences in the Nicolet and Bruker FTIR instruments and software, the most significant difference between these facilities is the IR source, so that OH absorption measurements with the Nicolet FTIR and its conventional IR source could not practically be made with apertures < 50–100 µm, while OH absorption bands could routinely be made with the Bruker FTIR and synchrotron IR source through a 10 µm aperture. In both cases, the IR sources are unpolarized, leading to differences in those OH absorption bands that are anisotropic in quartz and mica grains of varying orientation. Small sharp OH bands due to hydrogen interstitials of quartz (between 3595 and $3379\,\mathrm{cm^{-1}}$) and intrinsic OH bands of micas (at $\sim 3600\,\mathrm{cm^{-1}}$) are strongly anisotropic (Kats, 1962;

Beran, 2002). However, the primary OH band of interest for water weakening of milky quartz (at 3400 cm^{-1}) is broad and isotropic (Kekulawala et al., 1978; Aines et al., 1984), associated with dispersed fluid inclusions. Variations in absorbance of this band for neighboring quartz grains represent real variations in water content and not variations in quartz grain orientation.

Direct comparisons of intragranular water of a given quartz grain using the two FTIR facilities and a common aperture size could not be made because of (1) the poor signal-to-noise ratio of spectral measurements through a 10 μm aperture with the broad globar IR radiation, and (2) the inability to make spectral measurements for a 100 μm-apertured area with the narrow synchrotron IR beam (which is not much broader at the microscope stage than the 10 μm aperture). Samples with uniform OH contents might serve as standards to compare OH absorption bands for different spectrometers, irrespective of aperture size, but our observations indicate that OH contents of the quartz grains in the mylonites we measured are highly variable. Measurements through finer apertures led to larger variances in OH absorption bands, within grains as well as between neighboring grains.

We also observed larger-amplitude interference fringes in spectra measured with the synchrotron IR source than those observed in spectra measured with the globar IR source for a given sample. These fringes are caused by internal reflection within doubly polished, parallel-sided IR plates, and they have larger magnitudes for the highly collimated IR synchrotron beam than for the broad, confocal globar IR radiation.

3.3 Interference fringes

The appearance of interference fringes in spectra can be useful to determine the optical path length in thin samples, as long as their amplitude is small compared with vibrational absorption bands of interest, or they are distinguishable from absorption bands by their wavenumber spacing. Interference fringes are present in many spectra we collected for quartz mylonite plates (Fig. 2c, grains 1 and 8), which are of manageable size for our thicker samples and problematic for thinner samples.

Interference fringes were routinely observed for all samples measured with synchrotron IR radiation and the Bruker FTIR instrument. We therefore made use of these fringes to determine local sample plate thicknesses. For sample plates with large interference fringes, we attempted to reduce their size by tilting samples by 45° in the IR beam or using a Cassegrain objective lens with large numerical apertures (0.6). However, neither of these methods was effective in reducing amplitudes of some of the very large interference fringes sufficiently to detect small OH absorption bands. We had greater success reducing interference fringes by fitting them where the baseline was free of absorption bands, using

DatLab software (similar to fringe modeling of Clark and Moffatt, 1978; Pistorius and DeGrip, 2004; Konevskikh et al., 2015), and subtracting the model fringes from the spectral data. This improved the quality of spectra when interference fringes had modest amplitudes, but interference fringes for thin samples were very large and resulting backgrounds were sufficiently irregular that we could not resolve small OH absorption bands.

3.4 IR plate thickness and OH absorbance determinations

Mean IR plate thicknesses were determined by focusing on imperfections in the top and bottom specimen surfaces, recording the numerical graduations on the focusing knob of the IR microscope stage for each surface, and converting to vertical displacement.

Local IR plate thicknesses were also determined from interference fringes measured in spectra collected with the synchrotron–Bruker FTIR microscope system, where thickness t is given by

$$t = 1/(2n\delta\upsilon),\tag{1}$$

where n is the mean refractive index of quartz ($n = 1.55$) and $\delta\upsilon$ is the measured peak-to-peak fringe spacing (Stuart et al., 1996). The two measures of thickness were in agreement within resolution ($\sim 5\%$) for a given IR plate and location within the specimen, with thick IR specimens (~ 100 μm) showing real variations in local thickness of ± 10 μm and thin samples varying in local thickness from 4 to 8 μm.

IR spectra were collected and integrated absorbances of OH bands were measured above an assumed straight-line background, where backgrounds were fit and integration limits were chosen at the same wavenumber values, from ~ 3705 to 2880 cm^{-1} for OH bands of quartz grains and ~ 3702 to 3544 cm^{-1} for OH bands of micas (Fig. 3a). We are satisfied by our ability to separate, to first order, the OH absorption bands due to fluid inclusions in quartz and due to micas in MT samples, because IR spectra of coarse muscovite grains in MT mylonites consist of a single OH absorption band at 3620 cm^{-1} (Fig. 3b). This strong OH stretching band is well known from multiple spectroscopic studies of muscovite (Beran, 2002; Tokiwai and Nakashima, 2010a, b; Heller-Kallai and Lapides, 2015).

Our ability to distinguish OH absorbance due to fluid inclusions and micas in MCT samples, by contrast, is poor. In addition to the primary OH absorption bands of muscovite (Fig. 3c) and biotite (Fig. 3d) grains at 3638 and 3614 cm^{-1}, respectively, MCT muscovite spectra show smaller OH bands at 3311, 3146, and 3035 cm^{-1} and biotite spectra show shoulders at both sides of the primary OH absorption band (at ~ 3679 and ~ 3561 cm^{-1}) and significant OH bands at 3258, 3043, and 2829 cm^{-1}. All of these OH bands are anisotropic, and complexly so. The primary OH band of MCT muscovite at 3638 cm^{-1}, measured in polarized IR ra-
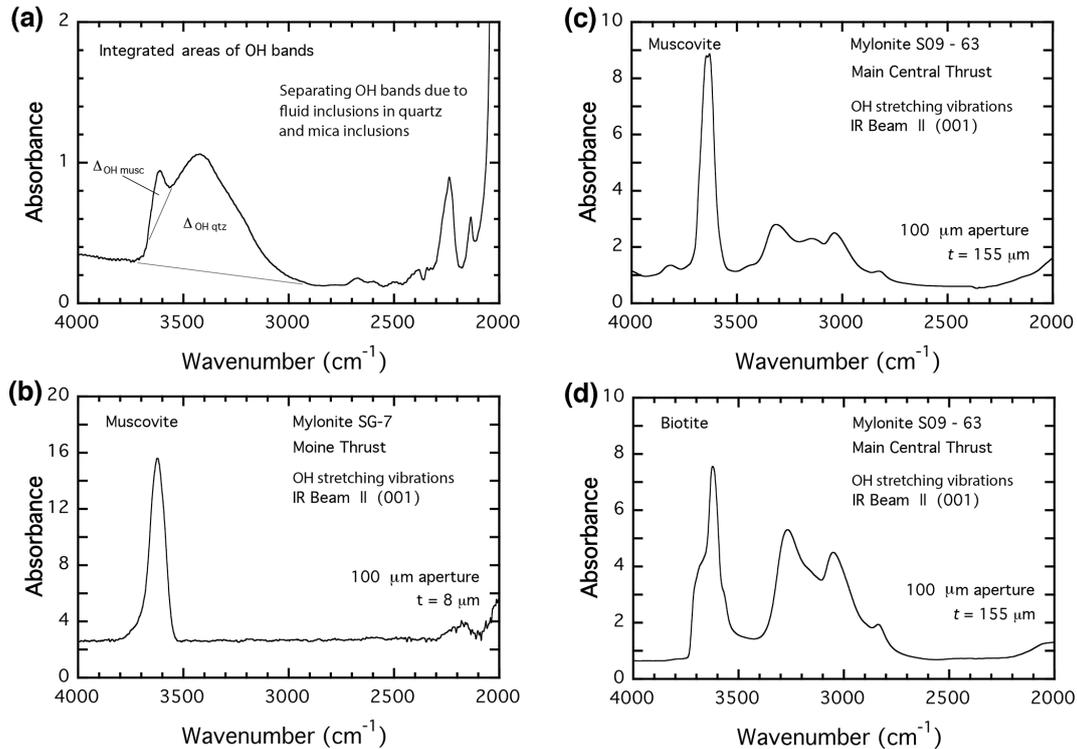
Figure 3. OH absorption spectra of quartz and mica grains. **(a)** IR spectrum of MT quartz grain (SG-10, Grain 2) with a broad $3400\,\mathrm{cm^{-1}}$ band due to fluid inclusions and a sharper OH band at $3600\,\mathrm{cm^{-1}}$ due to fine, intragranular mica inclusions. The integrated OH absorbances due to molecular water (and lesser hydrogen defects) of quartz ($\Delta_{\mathrm{OH\,qtz}}$ of the broad $3400\,\mathrm{cm^{-1}}$ band, in $\mathrm{cm^{-2}}$) and due to mica inclusions ($\Delta_{\mathrm{OH\,mica}}$ of the $3600\,\mathrm{cm^{-1}}$ band) can be distinguished using approximate straight-line fits. **(b)** IR spectrum of a large muscovite grain of MT sample SG-7. Muscovite grains in MT samples exhibit a simple spectrum with a prominent OH absorption band at $3620\,\mathrm{cm^{-1}}$ ($t = 8\,\mu\mathrm{m}$, absorbance normalized to $t = 0.1\,\mathrm{mm}$). **(c)** The prominent OH band of a large muscovite grain in MCT sample S09-63 ($t = 155\mathrm{um}$) appears at $3638\,\mathrm{cm^{-1}}$ with smaller OH bands at 3311, 3146, and $3035\,\mathrm{cm^{-1}}$. **(d)** The primary OH band of a large biotite grain in the same MCT sample appears at $3614\,\mathrm{cm^{-1}}$ (with shoulders at 3674 and $3561\,\mathrm{cm^{-1}}$) and secondary OH bands at 3258, 3043, and $2829\,\mathrm{cm^{-1}}$. The complex nature of secondary OH bands of MCT micas presents significant difficulties in separating OH absorptions of quartz grains due to molecular water and hydrogen defects from those of mica inclusions dispersed within quartz grains. All absorption spectra shown here were measured using unpolarized IR radiation with a conventional FTIR spectrometer and a $100\,\mu\mathrm{m}$ aperture. Absorbances for all spectra but **(b)** are normalized to a uniform thickness t of 1 mm.

diation, is strongest when the vibration direction E is parallel to the basal plane (001), consistent with idealized hydrogen positions in dioctahedral micas and the polarization of OH bands normally reported for muscovite (Beran, 2002). However, our polarized IR measurements of muscovite OH bands at 3311, 3146, and $3035\,\mathrm{cm^{-1}}$ indicate that they are nearly isotropic. The primary OH band of MCT biotite grains at $3614\,\mathrm{cm^{-1}}$ is strongest when E is perpendicular to (001), consistent with hydrogen positions of trioctahedral micas and OH band polarizations observed for phlogopite (Beran, 2002). However, the OH bands at 3258, 3043, and $2829\,\mathrm{cm^{-1}}$ are only weakly polarized and in the opposite sense of the primary $3614\,\mathrm{cm^{-1}}$ band.

As a result, we only feel confident in our determinations of OH absorbances of quartz grains in MCT mylonites (Fig. 2c), when mica inclusions are absent (the $3600\,\mathrm{cm^{-1}}$ band is undetectable). When the $3600\,\mathrm{cm^{-1}}$ band is present (Fig. 2d),

we cannot readily interpret absorption bands of molecular water or hydrogen defects in quartz; at best, quartz OH contents are overestimated.

Integrated absorbances of OH bands of quartz were used to determine OH contents based on the Beer–Lambert relation (Stuart et al., 1996),

$$A = kct, \tag{2}$$

where integrated absorbance $\Delta\ (= A / t$, determined in $\mathrm{cm^{-2}}$) is related to the concentration c of OH, assuming that k for the broad isotropic OH band at $3400\,\mathrm{cm^{-1}}$ due to fluid inclusions in milky quartz is the same as for the broad isotropic OH absorption band of molecular water in wet synthetic quartz (Aines et al., 1984):

$$c\ (\text{in molar ppm, } \mathrm{OH}/10^6\mathrm{Si}) = 1.05\Delta\ (\text{in cm}^{-2}). \tag{3}$$

To the extent that spectra include sharp OH absorption bands due to hydrogen point defects, this calibration will overesti-

mate OH concentrations due to H interstitials, given that the value of k for these bands is larger than for molecular water (Kats, 1962; Thomas et al., 2009) for quartz grains oriented for maximum OH absorbance (vibrational directions perpendicular to the c axis). However, apparent OH concentrations due to H interstitials will appear smaller for quartz grains oriented for minimum OH absorbance in unpolarized IR radiation. These errors are not serious for quartz grains with large molecular water contents that dominate over hydrogen point defect concentrations. However, we expect that our determinations of OH concentrations for dry quartz grains (< 100 ppm) with spectra dominated by sharp anisotropic OH bands are not as accurate as for wet quartz grains with spectra dominated by isotropic broad OH bands. We also acknowledge that the calibration for molecular water absorption of synthetic quartz used here differs from the calibration of the $3400\,\mathrm{cm}^{-1}$ OH band absorbance reported by Stipp et al. (2006) for milky quartz grains with fluid inclusions. If this alternative calibration is correct, OH contents reported here are smaller by a factor of 0.56. The calibration of Stipp et al. (2006) is based on FTIR measurements of individual grains of a pure quartzite and independent Karl Fischer titration of disaggregated quartz particles, and we do not understand the source of discrepancies in absorbance calibrations.

Integrated absorbances Δ were also measured for the $3600\,\mathrm{cm}^{-1}$ OH band of micas, but no attempt was made to convert these to OH (or mica inclusion) contents. Integrated OH absorbances due to unseen (below optical resolution) mica inclusions will depend on the path length through the micas, the mica orientations, and whether they consist of muscovite, biotite, or both within the volume measured.

3.5 Mapping OH absorption bands

Integrated areas of OH were measured as a function of spatial x and y dimensions within IR plates measured on the Bruker FTIR system, distinguishing absorbances of OH bands due to fluid and mica inclusions to the extent that this was possible. Samples were translated under the $10\,\mu\mathrm{m}$ IR beam using a motorized $x - y$ stage, controlled by OPUS software, and spectra were collected for each translation step, usually moving the stage by 10, or 30 or $50\,\mu\mathrm{m}$ in order to map larger regions (up to $\sim 4.5\,\mathrm{mm}^2$). Integrated absorbance measurements were made over 3705–$2880\,\mathrm{cm}^{-1}$ (to include the $3400\,\mathrm{cm}^{-1}$ broad band of milky quartz) and 3702–$3544\,\mathrm{cm}^{-1}$ (to determine the $3600\,\mathrm{cm}^{-1}$ mica band) for each scanned area (compiling absorbance measurements for 660 to 4950 spectra). The integrated absorbances of the $3600\,\mathrm{cm}^{-1}$ mica band were subtracted from the first of the two integrated absorbances to determine a representative measure of the OH bands of molecular water and hydrogen defects of quartz.

Given that the same IR background was used to reference all spectral measurements made during $x - y$ mapping of OH bands, long step-scan mapping projects were susceptible to

changes in aperture and condenser lens centering, IR beam drift, and beam outages while the synchrotron ring was refilled. As a result, we modified our IR absorbance measurement methods for step-scan mapping to obtain reasonably accurate integrated absorbances of broad OH bands without requiring high-resolution or precision measurements of small, sharp OH bands, with the goal of limiting total measurement times.

IR spectra used to map OH bands were made at a wavenumber resolution of $8\,\mathrm{cm}^{-1}$, reducing the interferometer mirror translation times with no detectable degradation in integrated absorbance measurements. More significantly, we reduced the number of scans to measure each IR spectrum from 512 to just 16, resulting in measurement times for each spectrum of only $\sim 10\,\mathrm{s}$. Tests of spectral quality with reduced numbers of scans indicated that integrated areas determined after 16 scans were within 8 % of values determined after 512 scans (for $\Delta \sim 3000\,\mathrm{cm}^{-2}$ and $t \sim 120\,\mu\mathrm{m}$). OH maps were constructed for sample areas of $0.066\,\mathrm{mm}^2$ ($22 \times 30 = 660$ spectra) to nearly $4.5\,\mathrm{mm}^2$ ($50 \times 99 = 4950$ spectra) requiring measurement times of $110\,\mathrm{min}$ to nearly $14\,\mathrm{h}$, respectively. The larger step-scan maps include some poor spectral data corresponding to beam drift or outages; these spectra were identified and removed from the data set.

Maps of integrated OH absorbance were contoured (using SigmaPlot) to form images of water contents and micas, and superposed on optical micrographs of the measured regions to look for correlations between OH content and microstructure. OH contents of quartz, due primarily to the broad $3400\,\mathrm{cm}^{-1}$ OH band of fluid inclusions and secondarily to sharp hydrogen defect bands, were mapped as molar ppm (OH/10^6Si), while the OH absorption band at $\sim 3600\,\mathrm{cm}^{-1}$ due to micas was mapped in units of integrated absorbance (cm^{-2}). Logarithmic contour intervals of $\log_{10}$(OH/10^6Si) were chosen to image water contents in quartz over a wide range of concentrations, and to provide visual images of water distributions at low (and high) values. OH contents were contoured in color with blue (and other cool colors) corresponding to large water contents, and red (and other warm colors) corresponding to low water contents. Logarithmic contours were also chosen to image distributions of micas, plotting $\log_{10}(\Delta)$ for the integrated absorbance of the $\sim 3600\,\mathrm{cm}^{-1}$ OH band, using a similar key for the contour interval, where cool colors correspond qualitatively to high mica contents and warm colors correspond to low mica contents.

4 Results

4.1 Synchrotron FTIR measurements

IR spectra of quartz in MT and MCT samples measured with the synchrotron–FTIR system through a $10\,\mu\mathrm{m}$ aperture (for samples $\sim 100\,\mu\mathrm{m}$ thick) exhibit OH absorption bands

of similar character as measured using a conventional FTIR system with a 100 μm aperture. OH bands of MT quartz grains generally include a large broad absorption band at 3400 cm^{-1} due to fluid inclusions, with some grains showing a secondary absorption band at 3600 cm^{-1} due to micas (Fig. 4a). Given the intense synchrotron IR source, we did not encounter any losses in spectral quality due to signal-to-noise ratios for the smaller sample volumes measured, though interference fringes are more apparent. Synchrotron FTIR measurements of MCT samples through a 10 μm aperture show the same sharp OH bands due to hydrogen point defects as measured for larger sampling volumes. With the exception of some unusual grains, broad OH bands at 3400 cm^{-1} in MCT samples are small to negligible.

Integrated absorbances of the broad 3400 cm^{-1} OH band measured with a 10 μm aperture are highly variable spatially, yielding water contents for individual spots within quartz grains for a given MT sample (SG-10) of 280 to 9000 ppm, with a comparable mean (2430 ppm) but more variance among individual measurements than measured with a 100 μm aperture (from 1130 to 8590 ppm for 45 measurements). For dry MCT samples (S09-71B), OH contents of quartz measured using a small (10 μm) aperture varied from 50 to 300 ppm, while OH contents measured with the larger (100 μm) aperture varied from 85 to 240 ppm. For unusually wet MCT samples (S09-35), OH contents of quartz measured using a small (10 μm) aperture varied from 150 to 7500 ppm, while OH contents measured with the larger (100 μm) aperture varied from 160 to 4620 ppm. The variations in size of sharp OH bands associated with hydrogen point defects, by comparison, are much smaller. The sizes of these absorption bands may be explained by differing quartz grain orientations without calling upon any variations in hydrogen point defect concentrations (Thomas et al., 2009).

4.2 Limits of IR plate thickness

IR spectra of quartz were measured through a 10 μm aperture, varying sample plate thickness from ∼ 100 to 4–8 μm, with the hope that we might be able to measure the OH bands of individual recrystallized grains in ultrathin IR plates. Owing to the coarse recrystallized grain sizes of MCT mylonites, we were able to measure IR spectra of most quartz grains in these samples for plate thicknesses of > 50 μm. However, our IR measurements of individual grains in MT samples (with recrystallized grains of ∼ 10–15 μm) are limited to larger porphyroclastic and deformed ribbon quartz grains. While the signal-to-noise ratio of our measurements continues to be acceptable to measure the small OH absorption bands in very thin IR plates, interference fringes increase in size as the IR plate thickness t is decreased. Interference fringes become very large at $t < 25$ μm and OH bands cannot be detected at $t = 13$ and 6.5 μm (Fig. 4b, c).

The magnitude of interference fringes can be modified by tilting the sample within the IR beam and increasing the nu-
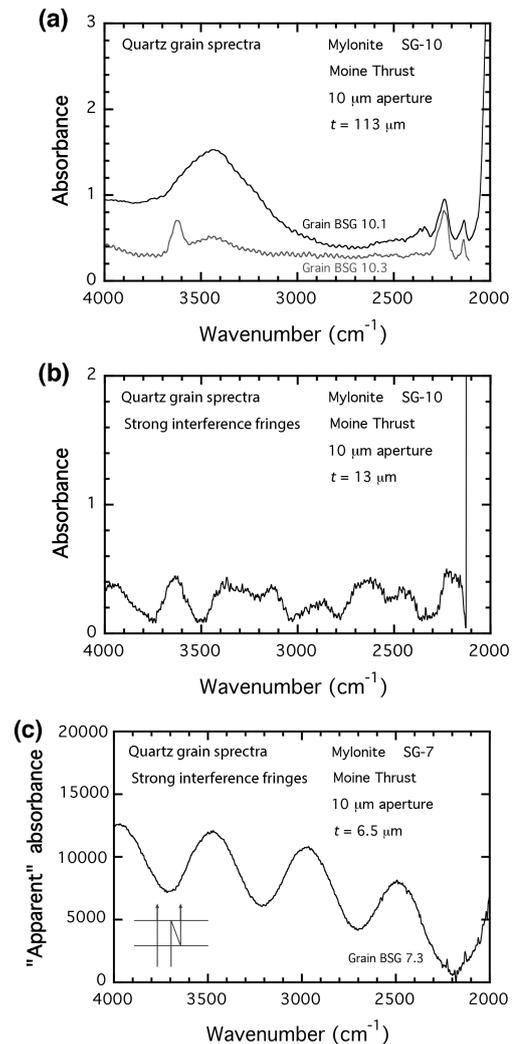

Figure 4. IR spectra of quartz grains in MT mylonite samples (Stack of Glencoul), measured with synchrotron–FTIR system using a 10 μm aperture with varying IR plate thicknesses (a) $t = 113$ μm (BSG 10, local plate thickness determined from interference fringes), (b) $t = 13$ μm (SG-10.2t), and (c) $t = 6.5$ μm (BSG 7.3, sample plate SG-7-1). (a) IR spectra of MT sample (SG-10) show OH absorption bands of similar character at the same wavenumbers for a 10 μm aperture as OH bands measured through a larger (100 μm) aperture, including a large broad absorption band at 3400 cm^{-1} due to dispersed fluid inclusions (both BSG 10.1 and BSG 10.3) and a sharper band at 3600 cm^{-1} due to mica inclusions (shown by BSG 10.3). Interference fringes in samples ∼ 100 μm thick are apparent, allowing determination of local IR plate thickness, but they do not obscure the OH absorption bands. (b) Interference fringes for samples < 25 μm thick are large, and make detection of small OH absorption bands difficult. The only detectable absorbance bands in sample SG-10.2t ($t = 13$ μm) are due to strong primary SiO vibrations (at $\upsilon < 2200$ cm^{-1}). (c) Interference fringes are very large for thin IR plates ($t = 6.5$ μm; SG-7-1); neither SiO nor OH absorption bands are observed, even after attempts to model them and remove fringes numerically. All absorbance values (and apparent absorbance values of interference fringes exhibited by SG-7) are normalized to a uniform sample thickness of 1 mm.

merical aperture of the Cassegrain objective on the IR microscope. However, with peak-to-trough fringe magnitudes 10^4 times greater than the OH bands in our mylonite samples, the modest reductions in fringe amplitude realized by these methods are not significant for the measurement of OH absorptions. Our efforts to model interference fringes were largely successful, reducing their magnitudes by a factor of ~ 100, but the resulting backgrounds were not flat enough at the scale of the known OH absorption bands of the MT (or MCT) samples to allow absorption band measurements for our thinnest sample plates. Interference fringes vary in magnitude according to IR plate thickness, surface polish, and scattering by internal flaws, but OH absorption bands could only be measured for samples of $\sim 40\,\mu$m thickness or greater.

4.3 Optical microstructures and plate thickness

Although the painstaking efforts to prepare ultrathin IR plates were not rewarded by spectral measurements of OH content within individual, finely recrystallized grains, optical imaging of deformation and recrystallization microstructures in ultrathin samples was improved over that using conventional thin sections. Optical microstructures of $100\,\mu$m thick IR plates are poorly resolved by comparison with those imaged in $30\,\mu$m thick sections (Fig. 1c, d), with interference colors that reflect greater optical retardation, grain boundaries that are not as clearly defined, and greater numbers of overlapping grains. Remarkably, ultrathin IR plates of quartz mylonites, just 4–8 μm thick (Fig. 1f), continue to exhibit contrast between grains and within grains, with first-order black to grey birefringence that can be enhanced by increasing image contrast.

High-magnification optical micrographs of ultrathin MT mylonites reveal microstructures (Fig. 5) that correspond better to TEM observations (Weathers et al., 1979; Ord and Christie, 1984) than to optical microstructures of conventional thin sections. While highly flattened ribbon quartz grains observed in $30\,\mu$m sections show smoothly varying undulatory extinction, ultrathin sections exhibit well developed subgrains within grain interiors, with sharply defined changes in extinction marking the locations of distinct subgrain walls (Fig. 5a). Prior TEM of MT mylonites revealed significant densities of free dislocations, which may be associated with smooth changes in extinction. However, TEM observations also show dense, sharply defined, low-angle subgrain walls (Weathers et al., 1979; Ord and Christie, 1984) that are often not resolved as optical microstructures in normal thin sections. These observations suggest that ultrathin sections may be useful to distinguish smooth changes in extinction (due to free dislocations and strains internal to subgrains) from discrete changes in extinction of overlapping and neighboring subgrains.

Recrystallized grains are apparent at some sutured grain boundaries in MT samples (Fig. 5a) with grain sizes that
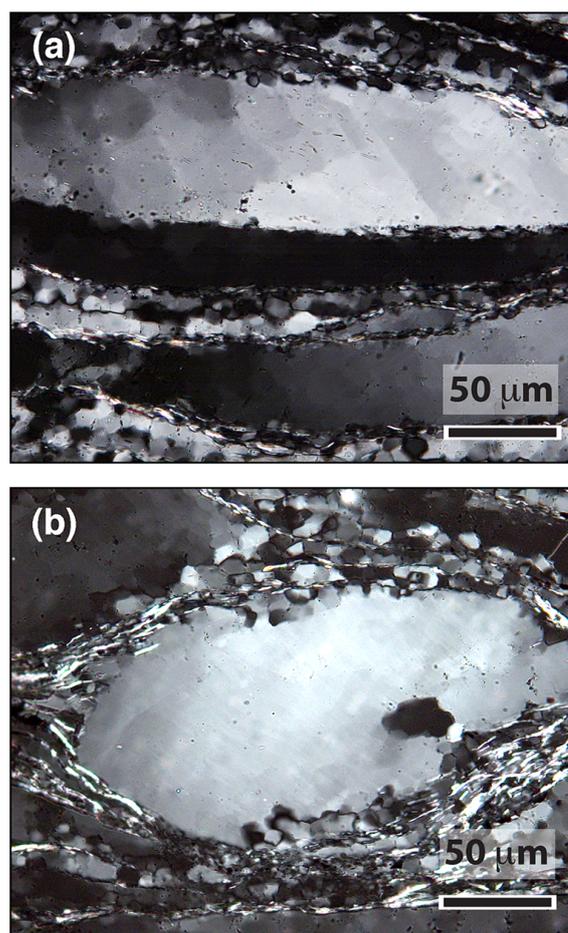

Figure 5. Ultrathin IR plates ($t = 4$–$8\,\mu$m) exhibit deformation microstructures in crossed-polarized light with greater clarity than those of conventional thin sections ($t = 30\,\mu$m). **(a)** Deformed ribbon quartz grains of MT sample SG-7-6 ($t = 6$–$8\,\mu$m) show distinct subgrains with sharply defined subgrain walls, while extinction in conventional thin sections of ribbon quartz is smoothly varying and subgrain boundaries are difficult to detect. Finely recrystallized quartz grains at sutured grain boundaries are smaller than subgrains within large deformed quartz grains. **(b)** Less deformed quartz porphyroclast of MT sample SG-7-5 ($t = 5$–$6\,\mu$m) with internal subgrains, and surrounding recrystallized quartz grains of similar dimensions to those of internal subgrains.

are significantly smaller than the dimensions of subgrains within the ribbon quartz grains. Microstructures of these new grains suggest that they form by grain boundary bulge mechanisms. Newly recrystallized grains surrounding other grains (Fig. 5b) have sizes in common with nearby subgrains, and the associated microstructures suggest that these recrystallized grains develop by subgrain rotation. While prior optical examination of MT mylonites using $30\,\mu$m thin sections has led to the conclusion that both BLG and SGR recrystallization were important during deformation (Law, 2014), quantitative evaluations of these processes and their contri-

butions to dislocation creep could be improved by the higher microstructural resolution offered by ultrathin sections.

4.4 High-resolution imaging of OH

By translating IR plates under the $10\,\mu m$ apertured IR beam and measuring spectra over many steps (spaced by 10 to $50\,\mu m$) we were able to compile integrated absorbances over spatial areas of up to $4.455\,mm^2$ ($50 \times 99 = 4950$ spectra, step size $= 30\,\mu m$). Integrated absorbances of OH bands were determined for the collection of spectra, choosing limits of 3705 to $2880\,cm^{-1}$ to include the broad OH band at $3400\,cm^{-1}$ and sharp OH bands between 3595 and $3379\,cm^{-1}$ due to fluid inclusions and hydrogen defects, respectively, within quartz grains. The integrated absorbance of the $3600\,cm^{-1}$ band of mica grains was determined (between 3702 and $3544\,cm^{-1}$) and subtracted from the first integrated absorbance of OH bands (as illustrated in Fig. 3a) to determine $\Delta_{OH\,qtz}$ of water and hydrogen defects of quartz grains.

These values were plotted spatially for MT and MCT samples, and contoured on common logarithm scales, to form high-resolution images (Figs. 6–9) of OH absorbance of quartz (converting to molar ppm, $OH/10^6 Si$) and OH absorbance of micas ($\Delta_{OH\,musc}$ in cm^{-2}). In all cases, we superposed the contoured OH maps on optical micrographs to make sense of OH distributions in terms of fluid inclusions, defects, and micas, and their relationships to deformation and recrystallization microstructures. Images of the $3600\,cm^{-1}$ mica OH absorbance were placed over plane light micrographs that highlight scattering (and sometimes color) due to micas, grain boundaries, and fluid inclusions, while images of OH absorbance due to fluid inclusions (principally the broad $3400\,cm^{-1}$ band at large integrated absorbances) and lesser hydrogen defects of quartz were placed over cross-polarized light micrographs that emphasize undulatory extinction, deformation microstructures and recrystallization of quartz grains.

FTIR maps of OH of quartz grains show that water contents of deformed mylonites (Figs. 6–8) are extremely heterogeneous when absorbance is dominated by the $3400\,cm^{-1}$ band, with water contents that vary from 300 to $> 10\,000$ ppm between neighboring grains and within grain interiors. This result helps explain the wide variations in water contents measured by conventional FTIR through a $100\,\mu m$ aperture. OH contents of quartz grains of relatively dry mylonites (Fig. 9) are more nearly constant (50–150 ppm) when IR spectra are dominated by sharp OH bands of hydrogen point defects. FTIR maps of mylonite samples, constructed for the $3600\,cm^{-1}$ OH absorbance, show that micas are heterogeneously distributed, with concentrations apparent at quartz grain boundaries in optical micrographs (Figs. 6–9) and finely dispersed micas within quartz grain interiors (Figs. 7, 8), some of which can be difficult to detect optically. We show these relationships in several contoured OH maps, focusing on different types of quartz grains and deformation microstructures.

While most quartz grains in MT mylonites are highly deformed, some quartz grains remained nearly equant (globular grains or quartz augen with c axes aligned perpendicular to foliation; Law et al., 1986), despite their high original OH contents in the form of fluid inclusions (Fig. 6). The lack of $3600\,cm^{-1}$ OH absorbances within globular quartz grains indicates that finely dispersed micas in original relict quartz grains are absent, while large $3600\,cm^{-1}$ OH absorbances at quartz grain extremities indicate that micas are localized at quartz grain boundaries (Fig. 6a, b). Broad-band OH contents of quartz of > 1000 ppm, thought to be sufficient for water weakening, are present in undeformed and deformed ribbon quartz grains (Fig. 6c, d) with very large water contents ($> 10\,000$ ppm) marking a healed crack in the quartz augen, made up of a planar array of fluid inclusions. OH contents due to fluid inclusions are also very large at the globular augen quartz boundaries, coincident with high mica concentrations, and in some ribbon and recrystallized quartz grains. With a sample plate thickness of $56\,\mu m$, these maps represent OH absorbances within the interiors of larger quartz grains, while OH absorbances of fine micas and recrystallized quartz represent composite spectra of polycrystalline fault rock. However, we are confident that the quartz OH contents reflect fluid inclusions, even in these fine-grained regions, because of the simple spectral quality of muscovite (Fig. 3) in the MT samples and our ability to distinguish between the 3400 and $3600\,cm^{-1}$ OH absorbances.

High-strain ribbon quartz grains in the MT samples have large OH contents (> 1000 ppm) comparable to those of water-weakened synthetic and milky quartz (samples SG-10 and SG-8, Figs. 7 and 8, respectively), with some reductions in OH at recrystallized margins of original grains. Micas, as imaged by the $3600\,cm^{-1}$ OH absorbance (Fig. 7a, b), continue to be highly localized at the grain boundaries of deformed quartz grains, with a mixture of fine-grained mica and quartz grains providing evidence for some redistribution during recrystallization (Fig. 8a, b). The broad $3400\,cm^{-1}$ OH absorbance in marginal recrystallized regions surrounding ribbon quartz grains are locally smaller than those of the original deformed quartz grains in some regions (Fig. 7c, d), while broad OH absorbances of recrystallized quartz continue to be large where mica contents (as evidenced by the $3600\,cm^{-1}$ band absorbance) are large (Fig. 8c, d).

FTIR maps of coarse-grained MCT mylonites yield spectral measurements of individual grains of quartz, muscovite, and biotite, even for relatively thick IR plates and larger step sizes (Fig. 9). MCT mica grains are readily detected by optical microscopy, and they are apparent as large OH contents based on the $3600\,cm^{-1}$ absorption band (Fig. 9a, b). Small, sharp absorption bands of quartz grains yield OH contents of ~ 100 ppm (Fig. 9c, d), with only local regions of quartz with larger OH contents near contacts with coarse-grained muscovite and biotite grains. Quartz grain interiors generally
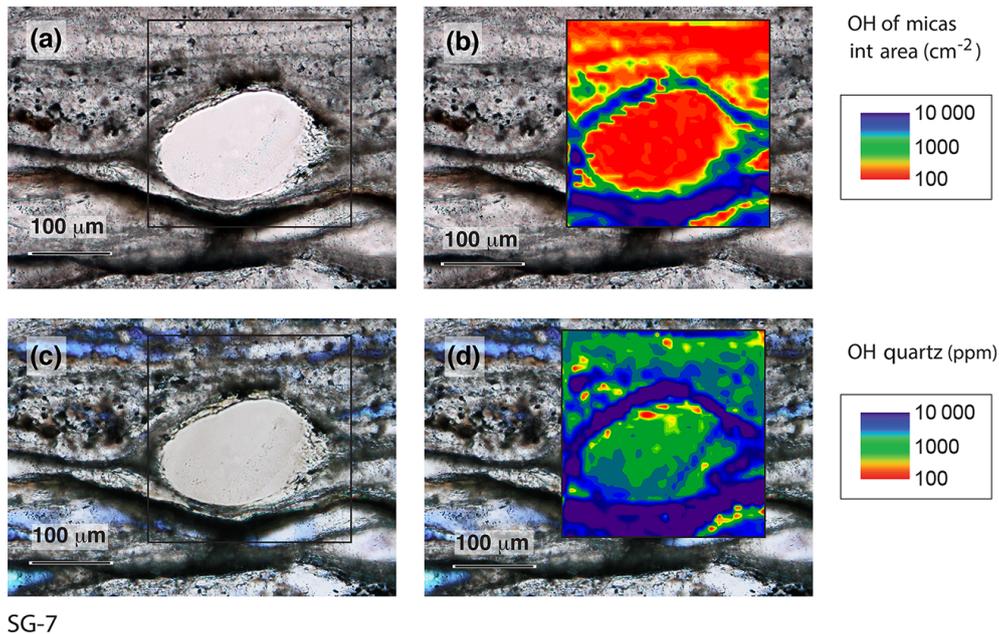
SG-7

Figure 6. OH absorbance maps of MT sample SG-7 constructed from 900 IR spectra (SG-7t-1map, 30×30 steps, $10 \,\mu m$ step^{-1}) for a doubly polished plate prepared ($56 \,\mu m$ thick) perpendicular to foliation and parallel to mineral lineation/transport direction (lineation horizontal in all panels). **(a)** Plane-polarized micrograph of IR plate SG-7t showing nearly equant globular augen quartz grain surrounded by highly deformed ribbon and recrystallized quartz grains. Light scattering is mostly due to micas and fluid inclusions. Outlined box is the region imaged by integrated IR absorbances. **(b)** The same plane-polarized light micrograph as in **(a)** with superposed map of OH absorbance of the 3600 cm^{-1} band due to micas (OH of micas in integrated area, cm^{-2}). Contours are given in $\log_{10}(\Delta$ in cm$^{-2})$ for the integrated absorbance of the ~ 3600 cm^{-1} OH band. **(c)** Cross-polarized light micrograph of the same region of IR plate SG-7t as shown in **(a)**, with subtle undulatory extinction of ribbon quartz shown in white and first-order interference colors. **(d)** The same cross-polarized light micrograph as in **(c)** with superposed map of OH absorbance of the broad 3400 cm^{-1} band due to molecular water in fluid inclusions (and smaller OH bands due to hydrogen defects) of quartz grains (OH of quartz in molar ppm, OH/10^{6}Si). Contours given in $\log_{10}$ (ppm) for integrated absorbance of the broad 3400 cm^{-1} OH band (and lesser sharp OH bands) of quartz. OH contents of quartz and those associated with micas are contoured in color with blue (and cool colors) corresponding to large water (OH) contents, and red (and warm colors) corresponding to low water (OH) contents.

lack the absorbance band at 3600 cm^{-1}; thus, there is no evidence for finely dispersed micas within these coarse-grained deformed (and recrystallized) quartz grains. Contours of integrated OH absorptions at 3400 cm^{-1} are considerably larger for coarse-grained micas and near their contacts with quartz grains. However, these bands cannot be attributed to fluid inclusions where they coincide with large 3600 cm^{-1} mica bands, given that muscovite and biotite grains in the MCT samples exhibit complex secondary OH bands between 3311 and 2829 cm^{-1}.

5 Discussion

Our IR spectra collected from quartz-rich mylonites in the footwall to the MT (Scottish Caledonides) and the hanging wall to the MCT (Himalaya of NW India) using synchrotron IR radiation through a 10 μm aperture are comparable to IR spectra we collected for the same samples using a conventional FTIR-microscope system through a 100 μm aperture. The broad OH band and large water contents of the MT my-

lonites deformed at 300–350 °C are in line with previous FTIR studies of OH in quartz deformed under greenschist facies conditions (Kronenberg et al., 1990; Gleason and De-Sisto, 2008). The sharp OH bands and low water contents of the MCT mylonites deformed at 535–735 °C are consistent with FTIR studies of quartz in other shear zones deformed at amphibolite conditions (Han et al., 2013; Kilian et al., 2016).

5.1 Limits on measurement volume

While synchrotron IR radiation has enabled spectral measurements through small apertured areas, we have not succeeded in measuring OH absorption bands for ultrathin samples when their interference fringes are larger than the absorption bands. Modeling interference fringes helped but was not sufficient to measure OH spectra of individual, recrystallized quartz grains of the MT. The physical means by which we attempted to reduce interference fringes (rotating the sample within the IR beam, and changing numerical aperture of the IR objective) were also unsuccessful. However, interference fringes might be reduced in future stud-
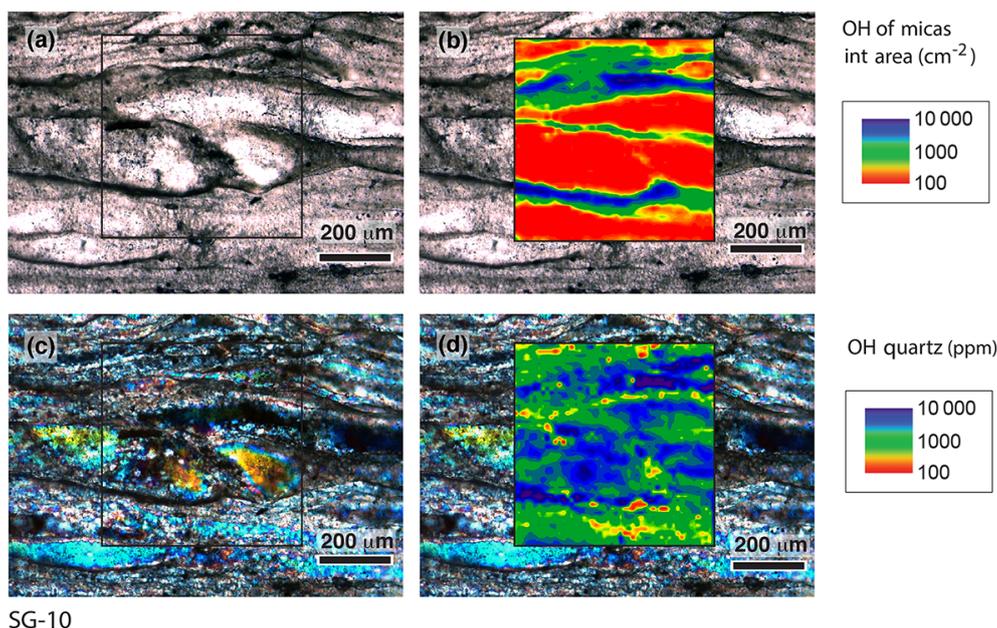
Figure 7. OH absorbance maps of MT sample SG-10 constructed from 3600 IR spectra (SG-10-XY2, 60×60 steps, $10\,\mu m\,step^{-1}$) for a doubly polished plate prepared ($117\,\mu m$ thick) perpendicular to foliation and parallel to mineral lineation/transport direction (lineation horizontal in all panels). **(a)** Plane-polarized micrograph of IR plate SG-10-2 showing deformed ribbon quartz grains surrounded by recrystallized quartz grains. **(b)** The same plane-polarized light micrograph as in **(a)** with superposed map of OH absorbance of the $3600\,cm^{-1}$ band due to micas. **(c)** Cross-polarized light micrograph of the same region of IR plate SG-10-2 as shown in **(a)**, with undulatory extinction of deformed ribbon quartz grains, incipient recrystallized grains at quartz ribbon margins, and recrystallized matrix grains shown by first-order interference colors. **(d)** The same cross-polarized light micrograph as in **(c)** with superposed map of OH absorbance of the broad $3400\,cm^{-1}$ band due to molecular water in fluid inclusions of quartz grains (OH of quartz in molar ppm, $OH/10^6 Si$). OH contents of quartz and micas are contoured in color using the same convention as in Fig. 6.

ies by a number of other methods. Interference fringes could be eliminated if ultrathin samples are mounted on a substrate with a matching refractive index n (S. Marti, personal communication, 2014). Such a substrate would need to be IR-transparent, facilitate bonding between the sample and substrate (by low-temperature melting or casting, to eliminate any residual air gaps between the sample and substrate), and lack OH bonds of its own. Alternatively, internal reflections could be reduced if thin samples are immersed in polychlorotrifluoroethylene oil ($n = 1.41$), which exhibits strong absorption bands at $< 2500\,cm^{-1}$ but has only small bands (between 3600 and $3200\,cm^{-1}$) that might interfere with OH absorptions of the sample (J. Mosenfelder and G. Rossman, personal communication, 2017). Internal reflections could also be reduced if only one surface of the ultrathin IR plate is polished, leaving the other surface precision-ground for a given plate thickness t (as employed by Woodhead et al., 1991). Spectra measured with just one polished surface will suffer some signal loss and spectra will need to be corrected for background. Another method of reducing interference fringes that obscure OH absorption bands might be developed by focused ion beam (FIB) milling of one side of a doubly polished sample to eliminate reflections at that surface over the IR wavenumbers of interest (R. Christoffersen, personal communication, 2014).

5.2 Wide variations in OH content

All previous FTIR studies of quartz mylonites have revealed large variations in water content for different grains within the same fault rock, and FTIR mapping of OH (Seaman et al., 2013, and this study) has revealed significant variations within grains. Our FTIR measurements of quartz OH contents using a $10\,\mu m$ aperture show that these variations depend on sampling volume, as observed by Kilian et al. (2016), who showed that broad OH band absorptions scale with size of the measurement area due to the inhomogeneous distributions of fluid inclusions.

The large and variable water contents of quartz mylonites are far above equilibrium solubilities (e.g., Paterson, 1986; Kronenberg et al., 1986; Cordier and Doukhan, 1989), and the variations in non-equilibrium OH content probably reflect some part of the history of water migration during deformation. Images of contoured OH absorbances of the broad $3400\,cm^{-1}$ band for quartz and the $3600\,cm^{-1}$ bands of micas constructed for MT and MCT samples show relationships with optical deformation and recovery microstructures that suggest mechanisms by which water is incorporated in quartz
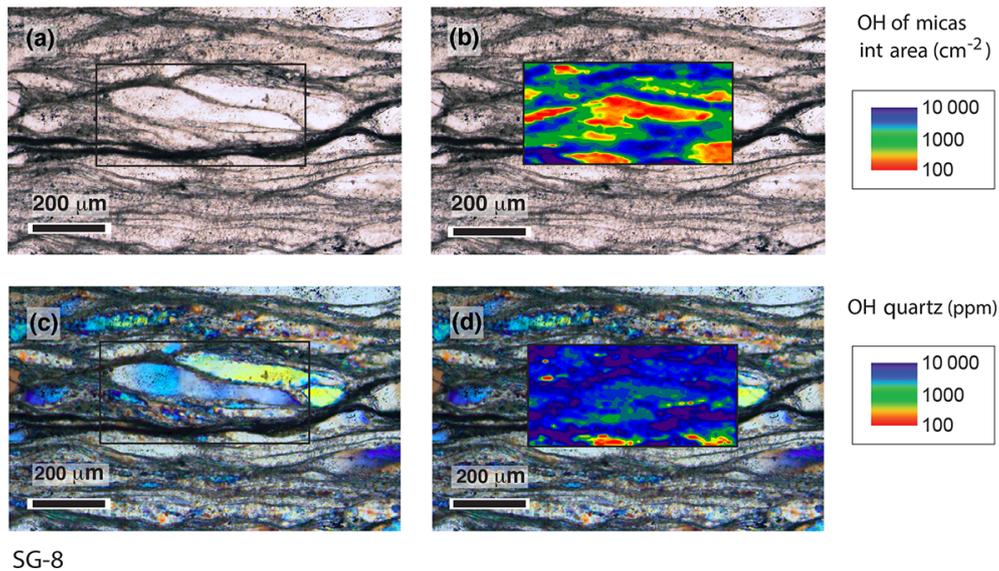
Figure 8. OH absorbance maps of MT sample SG-8 constructed from 1800 IR spectra (SG-8t-map1, 30×60 steps, $10\,\mu\text{m step}^{-1}$) for a doubly polished plate prepared (73 µm thick) perpendicular to foliation and parallel to mineral lineation/transport direction (lineation horizontal in all panels). **(a)** Plane-polarized micrograph of IR plate SG-8t showing deformed ribbon quartz grains and regions of finely dispersed mica and recrystallized quartz grains. **(b)** The same plane-polarized light micrograph as in **(a)** with superposed map of OH absorbance of the $3600\,\text{cm}^{-1}$ band due to micas. **(c)** Cross-polarized light micrograph of the same region of IR plate SG-8t as shown in **(a)**, with undulatory extinction of deformed ribbon quartz grains and regions of recrystallized grains shown by first-order interference colors. **(d)** The same cross-polarized light micrograph as in **(c)** with superposed map of OH absorbance of the broad $3400\,\text{cm}^{-1}$ band due to molecular water in fluid inclusions of quartz grains (OH of quartz in molar ppm, OH/10^6 Si). OH contents of quartz and micas are contoured in color using the same convention as in Fig. 6.

grain interiors, how water becomes redistributed during deformation and recovery, and how water is lost from quartz grain interiors.

OH contours within relatively undeformed quartz augen of the MT reveal planar zones of high water content that correspond to secondary fluid inclusions at healed microcracks (Fig. 6). We know little of this early brittle deformation, but these fluid inclusion arrays have microstructures similar to those generated during hydrothermal diffusional healing of cracks (Smith and Evans, 1984; Beeler and Hickman, 2015). As a result, early brittle deformation, infiltration of water along open cracks, and crack healing appear to be important to the early introduction of water to quartz grain interiors (Kronenberg et al., 1986, 1990; FitzGerald et al., 1991; Diamond et al., 2010; Tarantola et al., 2010, 2012; Stünitz et al., 2017).

OH contours in plastically deformed regions of MT samples are complex and water contents appear to vary with strain patterns and recrystallization (Figs. 6–8). Clearly defined planar arrays of course fluid inclusions are absent from these regions, although the measured high water contents indicate redistribution of water within quartz grains, rather than the loss of water. Processes of fluid inclusion decrepitation under deviatoric stresses have been studied experimentally (Diamond et al., 2010; Tarantola et al., 2010, 2012; Stünitz et al., 2017), and they include simultaneous shrink-

age of coarse ($> 10\,\mu\text{m}$, optical-scale) inclusions, generation of dislocations at fluid inclusion walls, and formation of a new population of very fine ($< 100\,\text{nm}$) fluid inclusions (visible only by transmission electron microscopy), which reside at dislocations and resemble water clusters and inclusions of deformed and heat-treated synthetic quartz (McLaren and Hobbs, 1972; White, 1973; Kirby and McCormick, 1979; Christie and Ord, 1980). The loss of coarse fluid inclusions and growth of fine inclusions require diffusive transport, which may occur along interconnected and mobile dislocations (McLaren et al., 1983, 1989; Cordier et al., 1988, 1994; Bakker and Jansen, 1990, 1994; Hollister, 1990; Kronenberg et al., 1990; Tarantola et al., 2010, 2012; Stünitz et al., 2017). Once formed, very fine fluid inclusions may also coarsen by pipe diffusion and processes documented by McLaren et al. (1983) and Cordier et al. (1988), leading to continuous changes in inclusion densities and size distributions.

Some regions of recrystallized quartz grains in MT samples appear to have somewhat lower OH contents than original ribbon quartz grains (Fig. 7), while highly recovered and recrystallized quartz grains in the MCT samples have little or no detectable molecular water (Fig. 9). Reductions in intragranular water during dynamic recrystallization have been attributed to sweeping of fluid inclusions by mobile grain boundaries and losses of water from the fault rock by rapid
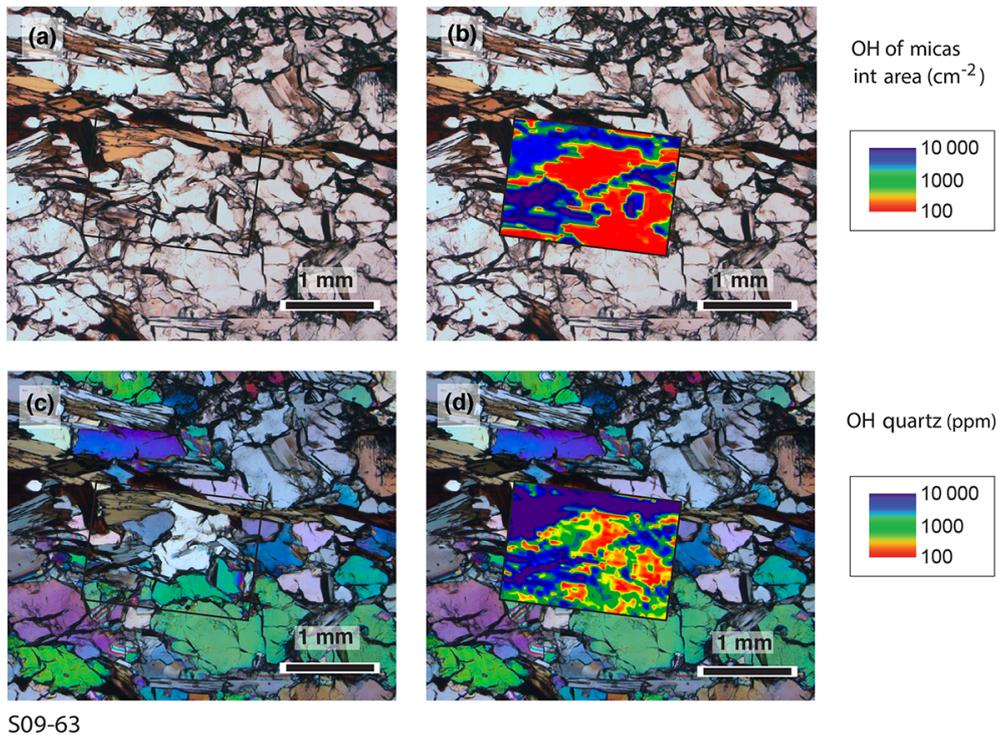
Figure 9. OH absorbance maps of MCT sample S09-63 constructed from 1200 IR spectra (S09-63-map1, 30×40 steps, $50\,\mu m\,step^{-1}$) for a doubly polished plate prepared ($155\,\mu m$ thick) perpendicular to foliation and parallel to mineral lineation/transport direction (lineation horizontal in all panels). **(a)** Plane-polarized micrograph of IR plate S-09-63 showing coarse, clear quartz grains, and coarse muscovite and biotite grains with readily distinguishable color and pleochroism. Scattering of light is primarily due to grain boundaries, with little evidence for dense fluid inclusions or finely dispersed micas within quartz grains. **(b)** The same plane-polarized light micrograph as in **(a)** with superposed map of OH absorbance of the $3600\,cm^{-1}$ band due to micas. **(c)** Cross-polarized light micrograph of the same region of IR plate SG-09-63 as shown in **(a)**, with high-temperature deformation and recovery microstructures (in higher-order interference colors) that are characterized by subtle (to absent) undulatory extinction of quartz, subgrain walls, and coarse recrystallized grains. **(d)** The same cross-polarized light micrograph as in **(c)** with superposed map of OH absorbance over 3705 and $2880\,cm^{-1}$ to capture the broad and sharp bands of quartz, deducting the large $3600\,cm^{-1}$ band of micas, but including smaller OH bands of micas between 3311 and $2920\,cm^{-1}$. Contours in this absorbance can only be attributed unambiguously to fluid inclusions and hydrogen defects in quartz where micas (and their $3600\,cm^{-1}$ absorbances) are absent. OH contents of quartz and micas are contoured in color using the same convention as in Fig. 6.

grain boundary diffusion (Faleiros et al., 2010; Seaman et al., 2013; Finch et al., 2016; Kilian et al., 2016).

5.3 Water weakening in nature?

This study adds to an emerging impression that quartz tectonites deformed at greenschist facies temperatures and natural strain rates are wet. Water contents of quartz mylonites from other locations within the MT zone deformed at greenschist facies conditions vary from 1400 to 7500 ppm (Kronenberg and Wolf, 1990). Water contents of deformed quartz across the Median Tectonic Line (Japan) vary from 300 to 2500 ppm (Nakashima et al., 1995), depending on metamorphic grade and shear displacement. Water contents of quartz deformed in granitic shear zones and mylonites at greenschist conditions reach values of 1100 and > 10 000 ppm (Gleason and DeSisto, 2008; Kronenberg et al., 1990).

The water contents of MT samples and other quartz mylonites deformed at greenschist conditions are comparable to (and even larger than) those of wet varieties of synthetic and natural milky quartz (350–4000 ppm) that exhibit water weakening in laboratory studies (e.g., Griggs and Blacic, 1965; Kekulawala et al., 1978; Stünitz et al., 2017). Highly deformed ribbon quartz grains, less deformed quartz augen, and recrystallized quartz grains of the MT exhibit OH bands of similar character to those of quartzites deformed in laboratory experiments, a result that validates applications of wet quartzite rheologies to evaluate rates of dislocation creep in middle to upper crustal shear zones (e.g., Hirth et al., 2001; Behr and Platt, 2011; Law, 2014).

In contrast, water contents of highly sheared and recrystallized quartz in the hanging wall of MCT samples and other mylonites deformed at amphibolite conditions are much smaller than measured for wet varieties of quartz deformed under greenschist facies conditions. Large shear strains accu-

mulated over ∼ 150–250 km of displacement along the MCT (e.g., Srivastava and Mitra, 1994; Hodges, 2000; Mitra et al., 2010; Tobgay et al., 2012; Law et al., 2013) and yet quartz OH contents (50–150 ppm) in our MCT samples are far lower than required for water weakening, thereby challenging our understanding of dislocation creep and the role of water in deformation deep in the continental crust. With only a few exceptions, IR spectra of our MCT samples have OH bands of the same character and size as dry natural quartz crystals, which are strong and have not been deformed by dislocation processes in laboratory experiments (e.g., Heard and Carter, 1968; Blacic, 1975; Blacic and Christie, 1984).

The low water contents of MCT quartz grains are consistent with the results of other IR studies of quartz deformed at amphibolite facies conditions (Nakashima et al., 1995; Han et al., 2013; Kilian et al., 2016). Han et al. (2013) reported water contents of just 10 to 110 ppm for quartz grains of granitic mylonites deformed at 400–500 °C within the Longmenshan tectonic zone (Sichuan, China). Kilian et al. (2016) measured OH contents of just 20 to 100 ppm for quartz grains of granitic mylonites deformed at upper amphibolite conditions (Truzzo meta-granite, Central Alps, Italy), with IR spectra dominated by sharp OH bands due to hydrogen point defects and no detectable broad band due to molecular water. Nakashima et al. (1995) found that quartz water contents of Sambagawa metamorphic rocks (Shikoku, Japan) depend on metamorphic grade, with the lowest water contents measured for rocks subjected to the highest temperatures.

Significant water contents (1400–4400 ppm) have been observed for quartz deformed at amphibolite conditions in mylonites of the El Pichao shear zone (NW Argentina), though reductions in water content are evident with progressive deformation (Finch et al., 2016). Fluid inclusions may be lost and intragranular water contents reduced during high temperature deformation by a variety of processes, ranging from pipe diffusion (Bakker and Jansen, 1990, 1994; Hollister, 1990; Cordier et al., 1994; Mavrogenes and Bodnar, 1994) to recrystallization and grain boundary sweeping (Faleiros et al., 2010; Seaman et al., 2013; Finch et al., 2016; Kilian et al., 2016), and partial melting (Seaman et al., 2013).

Given sufficiently high temperatures, it is possible that quartz may deform at tectonic strain rates without critical hydrogen defects at dislocations and water weakening (Kilian et al., 2016). However, this implies that we have not measured flow laws for appropriately dry quartzites that we can apply to amphibolite conditions and natural strain rates. Alternatively, water may have been lost from quartz interiors following deformation. It is also possible that hydrogen defects that enhance dislocation motion at high temperatures and natural strain rates may be sourced from grain boundaries or micas, diffusing over longer distances than are possible at greenschist conditions or laboratory strain rates.

Spatial variations in OH content of quartz in natural shear zones, as mapped in this study, may provide key insights into the role of water weakening and changes in water content during deformation and recrystallization. High-resolution FTIR imaging of OH in MT and MCT samples shows that water contents are increased, fluid inclusions are redistributed, and water contents are decreased during brittle deformation, plastic creep, recovery, and recrystallization. Changes in OH contents of quartz mylonites and the history of fluid migration during deformation may lead to changes in governing flow laws, non-steady rates of creep, and shifting zones of localized shear.

6 Conclusions

The brightness of synchrotron IR radiation enables measurement of IR spectra for much smaller sampling volumes than is possible using conventional globar IR sources of FTIR instruments. In this study, we have used this improvement in signal to characterize and measure small OH absorption bands in quartz mylonites with an aperture size of 10 μm and to map water contents spatially. The ability to measure IR spectra for small, individual recrystallized grains by methods described in this study is limited by samples that must be > 40 μm thick to avoid internal reflections that lead to interference fringes that are larger than OH absorption bands. High-resolution images of OH in quartz mylonites, based on spectra collected through a 10 μm aperture as samples are translated under the beam, reveal large variations in OH content that correspond to the distributions of fluid inclusions and layer silicates, and to deformation and recrystallization microstructures. The OH contents of quartz in MT mylonites deformed at greenschist conditions are comparable to wet quartzites deformed in the laboratory by processes of water weakening. By comparison, OH contents of quartz in MCT mylonites deformed at amphibolite conditions are small, and molecular water, as required to deform quartz at experimental strain rates, is absent. What role water plays in deformation at these conditions is unclear, calling for further studies of water weakening in natural shear zones. High-resolution FTIR mapping of OH offers a new method of tracking changes in water content during deformation, recovery, and recrystallization.

Competing interests. The authors declare that they have no conflict of interest.

References

Aines, R. D. and Rossman, G. R.: Water in minerals? a peak in the infrared, J. Geophys. Res., 89, 4059–4071, 1984.

Aines, R. D., Kirby, S. H., and Rossman, G. R.: Hydrogen speciation in synthetic quartz, Phys. Chem. Miner., 11, 204–212, 1984.

Baeta, R. D. and Ashby, K. H. G.: Mechanical deformation of quartz I. constant strain-rate compression experiments, Phil. Mag., 22, 601–623, 1970.

Bai, Q. and Kohlstedt, D. L.: Effects of chemical environment on the solubility and incorporation mechanism for hydrogen in olivine, Phys. Chem. Miner., 19, 460–471, 1996.

Bakker, R. J. and Jansen, J. B. H.: Preferential water leakage from fluid inclusions by means of mobile dislocations, Nature, 345, 58–60, 1990.

Bakker, R. J. and Jansen, J. B. H.: A mechanism for preferential H_2O leakage from fluid inclusions in quartz, based on TEM observations, Contrib. Mineral. Petrol., 116, 7–20, 1994.

Beeler, N. M. and Hickman, S. H.: Direct measurement of asperity contact growth in quartz at hydrothermal conditions, J. Geophys. Res., 120, 3599–3616, https://doi.org/10.1002/2014JB011816, 2015.

Behr, W. M. and Platt, J. P.: A naturally constrained stress profile through the middle crust in an extensional terrane, Earth Planet. Sc. Lett., 303, 181–192, https://doi.org/10.1016/j.epsl.2010.11.044, 2011.

Beran, A.: Infrared spectroscopy of micas, in: Micas: Crystal Chemistry and Metamorphic Petrology, Reviews in Mineralogy and Geochemistry, v. 46, edited by: Mottana, A., Sassi, F. P., Thompson Jr., J. B., Guggenheim, S., Mineral. Soc. Amer., P. H. Ribbe Series Editor, Mineral. Soc. America, Washington, DC., chap. 7., 351–369, 2002.

Blacic, J. D.: Plastic deformation mechanisms in quartz: the effect of water, Tectonophysics, 27, 271–294, 1975.

Blacic, J. D.: Water diffusion in quartz at high pressure: tectonic implications, Geophys. Res. Lett., 8, 721–723, 1981.

Blacic, J. D. and Christie, J. M.: Plasticity and hydrolytic weakening of quartz single crystals, J. Geophys. Res., 89, 4223–4239, 1984.

Bonney, T.: Notes on some rocks collected by C. Callaway, Quarterly Journal of the Geological Society of London, 39, 414–422, 1883.

Butler, R. W. H.: The role of thrust tectonic models in understanding structural evolution in NW Scotland, in: Continental Tectonics and Mountain Building: The Legacy of Peach and Horne, edited by: Law, R. D., Butler, R. W. H., Holdsworth, R. E., Krabbendam, M., and Strachan R. A., Geological Society, London, Special Publications, 335, 293–320, https://doi.org/10.1144/SP335.14, 2010.

Carr, G. L., Smith, R. J., Mihaly, L., Zhang, H., Reitze, D. H., and Tanner, D. B.: High-resolution far-infrared spectroscopy at NSLS beamline U121R, Infrared Physics and Technology, 51, 404–406, https://doi.org/10.1016/j.infrared.2007.12.034, 2008.

Chernak, L. J., Hirth, G., Selverstone, J., and Tullis, J.: Effects of aqueous and carbonic fluids on the dislocation creep strength of quartz, J. Geophys. Res., 114, B04201, https://doi.org/10.1029/2008JB005884, 2009.

Christie, J. M.: Mylonitic rocks of the Moine Thrust-zone in the Assynt region, north-west Scotland, Trans. Geol. Soc. Edinburgh, 18, 79–93, 1960.

Christie, J. M.: The Moine thrust zone in the Assynt region, northwest Scotland, University of California Publication Geological Science, 40, 345–440, 1963.

Christie, J. M. and Ord, A.: Flow stress from microstructures of mylonites: example and current assessment, J. Geophys. Res., 85, 6253–6262, 1980.

Christie, J. M., McIntyre, D. B., and Weiss, L. E.: Appendix to McIntyre, D. B.: The Moine thrust – its discovery, age and tectonic significance, Proceedings of the Geologists' Association, 65, 219–220, 1954.

Clark, F. R. S. and Moffatt, D. J.: The elimination of interference fringes from infrared spectra, Appl. Spectrosc., 32, 547–549, 1978.

Cordier, P. and Doukhan, J.-C.: Water solubility in quartz and its influence on ductility, Eur. J. Mineral., 1, 221–237, 1989.

Cordier, P. and Doukhan, J.-C.: Water speciation in quartz: a near infrared study, Am. Mineral., 76, 361–369, 1991.

Cordier, P., Boulogne, B., and Doukhan, J.-C.: Water precipitation and diffusion in wet quartz and wet berlinite, $AlPO_4$, B. Mineral., 111, 113–137, 1988.

Cordier, P., Weil, J. A., Howarth, D. F., and Doukhan, J.-C.: Influence of the $(4H)_{Si}$ defect on dislocation motion in crystalline quartz, Eur. J. Mineral., 6, 17–22, 1994.

Dewey, J. F., Dalziel, I. W. D., Reavy, R. J., and Strachan, R. A.: The neoproterozoic to mid-Devonian evolution of Scotland: a review and unresolved issues, Scottish J. Geol., 51, 5–30, https://doi.org/10.1144/sjg2014-007, 2015.

Diamond, L. W., Tarantola, A., and Stünitz, H.: Modification of fluid inclusions in quartz by deviatoric stress, II: experimentally induced changes in inclusion volume and composition, Contrib. Mineral. Petr., 160, 845–864, https://doi.org/10.1007/s00410-010-0510-6, 2010.

Elliot, D. and Johnson, M. R. W.: The structural evolution of the northern part of the Moine thrust zone, T. Roy. Soc. Edin.-Earth, 71, 69–96, 1980.

Faleiros, F. M., Campanha, G. A. C., Bello, R. M. S., and Fuzikawa, K.: Quartz recrystallization regimes, c-axis texture transitions and fluid inclusion reequilibration in a prograde greenschist to amphibolite facies mylonite zone (Ribeira Shear Zone, SE Brazil), Tectonophysics, 485, 193–214, https://doi.org/10.1016/j.tecto.2009.12.014, 2010.

Finch, M. A., Weinberg, R. F., and Hunter, N. J. R.: Water loss and the origin of thick ultramylonites, Geology, 44, 599–602, https://doi.org/10.1130/G37972.1, 2016.

FitzGerald, J. D., Boland, J. N., McLaren, A. C., Ord, A., and Hobbs, B. E.: Microstructures in water-weakened single crystals of quartz, J. Geophys. Res., 96, 2139–2155, 1991.

Francsis, M. K.: Piezometry and Strain Rate Estimates along Mid-crustal Shear Zones, MS thesis, Virginia Tech, USA, available at: http://scholar.lib.vt.edu/theses/available/etd-05032012-162325/ (last access: 26 June 2017), 2012.

Gerretsen, J., Paterson, M. S., and McLaren, A. C.: The uptake and solubility of water in quartz at elevated pressure and temperature, Phys. Chem. Min., 16, 334–342, 1989.

Gleason, G. C. and DeSisto, S.: A natural example of crystal-plastic deformation enhancing the incorporation of water into quartz, Tectonophysics, 446, 16–30, https://doi.org/10.1016/j.tecto.2007.09.006, 2008.

Gleason, G. C. and Tullis, J.: A flow law for dislocation creep of quartz aggregates determined with the molten-salt cell, Tectonophysics, 247, 1–23, 1995.

Godin, L., Grujic, D., Law, R. D., and Searle, M. P.: Channel flow, ductile extrusion and exhumation in continental collision zones: an introduction, in: Channel Flow, Ductile Extrusion and Exhumation in Continental Collision Zones, edited by: Law, R. D., Searle, M. P., and Godin, L., Geological Society, London, Special Publications, 268, 1–23, https://doi.org/10.1144/GSL.SP.2006.268.01.01, 2006.

Grasemann, B., Fritz, H., and Vannay J. C.: Quantitative kinematic flow analysis from the Main Central Thrust Zone (NW-Himalaya, India): implications for a decelerating strain path and the extrusion of orogenic wedges, J. Struct. Geol., 21, 837–853, https://doi.org/10.1016/S0191-8141(99)00077-2, 1999.

Griggs, D. T.: Hydrolytic weakening of quartz and other silicates, Geophys. J. Roy. Astr. S., 14, 19–31, 1967.

Griggs, D. T.: A model of hydrolytic weakening in quartz, J. Geophys. Res., 79, 1653–1661, 1974.

Griggs, D. T. and Blacic, J. D.: Quartz: anomalous weakness of synthetic crystals, Science, 147, 292–295, 1965.

Grujic, D., Casey, M., Davidson, C., Hollister, L. S., Kundig, K. Pavlis, T., and Schmid, S.: Ductile extrusion of the Higher Himalayan crystalline in Bhutan: evidence from quartz microfabrics, Tectonophysics, 260, 21–43, https://doi.org/10.1016/0040-1951(96)00074-1, 1996.

Han, L., Zhou, Y. S., and He, C. R.: Water-enhanced plastic deformation in felsic rocks, Science China-Earth Sciences, 56, 203–216, https://doi.org/10.1007/s11430-012-4367-6, 2013.

Heard, H. C. and Carter, N. L.: Experimentally induced "natural" intragranular flow in quartz and quartzite, Am. J. Sci., 266, 1–42, 1968.

Heilbronner, R, and Barrett, S.: Image Analysis in Earth Sciences, Microstructures and Textures of Earth Materials, Springer Verlag, Heidelberg, 520 pp., 2014.

Heller-Kallai, L. and Lapides, I.: Dehydroxylation of muscovite: study of quenched samples, Phys. Chem. Miner., 42, 835–845, 2015.

Hirsch, P. B.: A mechanism for the effect of doping on dislocation mobility, J. Phys. Colloque ,C6 40, C6-117–C6-121, 1979.

Hirth, G. and Tullis, J.: Dislocation creep regimes in quartz aggregates, J. Struct. Geol., 14, 145–159, 1992.

Hirth, G., Teyssier, C., and Dunlap, W. J.: An evaluation of quartzite flow laws based on comparisons between experimentally and naturally deformed rocks, Int. J. Earth Sci., 90, 77–87, 2001.

Hobbs, B. E.: Recrystallization of single crystals of quartz, Tectonophysics, 6, 353–401, 1968.

Hobbs, B. E.: The influence of metamorphic environment upon the deformation of minerals, Tectonophysics, 78, 335–383, 1981.

Hodges, K. V.: Tectonics of the Himalaya and southern Tibet from two perspectives, Geol. Soc. Am. Bull., 112, 324–350, https://doi.org/10.1130/0016-7606(2000)112<0324:TOTHAS>2.3.CO;2, 2000.

Hollister, L. S.: Enrichment of CO_2 in fluid inclusions in quartz by removal of H_2O during crystal-plastic deformation, J. Struct. Geol., 12, 895–901, 1990.

Holyoke III, C. W., and Kronenberg, A. K.: Accurate differential stress measurement using the molten salt cell and solid salt assemblies in the Griggs apparatus with application to strength, piezometers and rheology, Tectonophysics, 494, 17–31, https://doi.org/10.1016/j.tecto.2010.08.001, 2010.

Holyoke III, C. W. and Kronenberg, A. K.: Reversible water weakening of quartz, Earth Planet. Sc. Lett., 374, 185–190, https://doi.org/10.1016/j.epsl.2013.05.039, 2013.

Jaoul, O., Tullis, J., and Kronenberg, A. K.: The effect of varying water contents on the creep behavior of Heavitree quartzite, J. Geophys. Res., 89, 4298–4312, 1984.

Johnson, M. R. W., Kelly, S. P., Oliver, G. J. H., and Winter, D. A.: Thermal effects and timing of thrusting n the Moine thrust zone, J. Geol. Soc. London, 142, 863–874, 1985.

Kats, A.: Hydrogen in alpha quartz, Philips Research Reports, 17, 1–31, 133–195, 201–279, 1962.

Kekulawala, K. R. S. S., Paterson, M. S., and Boland, J. N.: Hydrolytic weakening in quartz, Tectonophysics, 46, T1–T6, 1978.

Kekulawala, K. R. S. S., Paterson, M. S., and Boland, J. N.: An experimental study of the role of water in quartz deformation, in: Mechanical Behavior of Crustal Rocks (The Handin Volume), edited by: Carter, N. L., Friedman, M., Logan, J. M., and Stearns, D. W., Geophys. Monograph 24, Amer. Geophys. Union, Washington, DC, 49–60, 1981.

Kilian, R., Heilbronner, R., Holyoke III, C. W., Kronenberg, A. K., and Stünitz, H.: Dislocation creep of dry quartz, J. Geophys. Res., 121, 3278–3299, https://doi.org/10.1002/2015JB012771, 2016.

Kirby, S. H. and McCormick, J. W.: Creep of hydrolytically weakened synthetic quartz crystals oriented to promote 2110 <0001> slip: a brief summary of work to date, B. Mineral., 102, 124–137, 1979.

Kohlstedt, D. L., Keppler, H., and Rubie, D. C.: Solubility of water in the α, β and γ phases of $(Mg,Fe)_2SiO_4$, Contrib. Mineral. Petrol., 123, 345–357, 1996.

Konevskikh, T., Ponossov, A., Blümel, R., Lukacs, R., and Kohler, A.: Fringes in FTIR spectroscopy revisted: understanding and modeling fringes in infrared spectroscopy of thin films, Analyst, 140, 3969–3980, https://doi.org/10.1039/c4an02343a, 2015.

Kronenberg, A. K. and Tullis, J.: Flow strengths of quartz aggregates: grain size and pressure effects due to hydrolytic weakening, J. Geophys. Res., 89, 4281–4297, 1984.

Kronenberg, A. K. and Wolf, G. H.: FTIR determinations of intragranular water content in quartz-bearing rocks: implications for hydrolytic weakening in the laboratory and within the Earth, Tectonophysics, 172, 255–271, 1990.

Kronenberg, A. K., Kirby, S. H., Aines, R. D., and Rossman, G. R.: Solubility and diffusional uptake of hydrogen in quartz at high water pressures: implications for hydrolytic weakening, J. Geophys. Res., 91, 12723–12744, 1986.

Kronenberg, A. K., Segall, P., and Wolf, G. H.: Hydrolytic weakening and penetrative deformation within a natural shear zone, in: The Brittle-Ductile Transition in Rocks (The Heard Volume), edited by: Duba, A. G., Durham, W. B., Handin, J. W., and Wang, H. F., Geophys. Monograph 56, Amer. Geophys. Union, Washington, DC, 21–36, 1990.

Kruhl, J. H.: Reply: Prism- and basal-plane parallel subgrain boundaries in quartz: a microstructural geothermobarometer, J. Metamor. Geol., 16, 142–146, 1998.

Law, R. D.: Moine Thrust zone mylonites at the Stack of Glencoul: II – results of vorticity analyses and their tectonic significance, in: Continental Tectonics and Mountain Building: The Legacy of Peach and Horne, edited by: Law, R. D., Butler, R. W. H., Holdsworth, R. E., Krabbendam, M., and Strachan R. A., Geological Society, London, Special Publications, 335, 579–602, https://doi.org/10.1144/SP335.23, 2010.

Law, R. D.: Deformation thermometry based on quartz c-axis fabrics and recrystallization microstructures: A review, J. Struct. Geol., 66, 129–161, https://doi.org/10.1016/j.jsg.2014.05.023, 2014.

Law, R. D. and Johnson, M. R. W.: Microstructures and crystal fabrics of the Moine Thrust zone and Moine Nappe: history of research and changing tectonic interpretations, in: Continental Tectonics and Mountain Building: The Legacy of Peach and Horne, edited by: Law, R. D., Butler, R. W. H., Holdsworth, R. E., Krabbendam, M., and Strachan R. A., Geological Society, London, Special Publications, 335, 443–503, https://doi.org/10.1144/SP335.21, 2010.

Law, R. D., Casey, M., and Knipe, R. J.: Kinematic and tectonic significance of microstructures and crystallographic fabrics within quartz mylonites from the Assynt and Eriboll regions of the Moine thrust zone, NW Scotland, T. Roy. Soc. Edin.-Earth, 77, 99–125, 1986.

Law, R. D., Mainprice, D., Casey, M., Lloyd, G. E., Knipe, R. J., Cook, B., and Thigpen, J. R.: Moine Thrust zone mylonites at the Stack of Glencoul: 1 – microstructures, strain and influence of recrystallization on quartz crystal fabric development, in: Continental Tectonics and Mountain Building: The Legacy of Peach and Horne, edited by: Law, R. D., Butler, R. W. H., Holdsworth, R. E., Krabbendam, M., and Strachan R. A., Geological Society, London, Special Publications, 335, 543–577, https://doi.org/10.1144/SP335.23, 2010.

Law, R. D., Stahr III, D. W., Francsis, M. K., Ashley, K. T., Grasemann, B., and Ahmad, T.: Deformation temperatures and flow vorticities near the base of the Greater Himalayan Series, Sutlej Valley and Shimla Klippe, NW India, J. Struct. Geol., 54, 21–53, 2013.

Linker, M. F., Kirby, S. H., Ord, A., and Christie, J. M.: Effects of compression direction on the plasticity and rheology of hydrolytically weakened synthetic quartz crystals at atmospheric pressure, J. Geophys. Res., 89, 4241–4255, 1984.

Lister, G. S.: Crossed-girdle c-axis fabrics in quartzites plastically deformed by plane strain and progressive simple shear, Tectonophysics, 39, 51–54, https://doi.org/10.1016/0040-1951(77)90087-7, 1977.

Lobo, R. P. S. M., LaVeigne, J. D., Reitze, D. H., Tanner, D. B., and Carr, R. L.: Performance of new infrared beamline U121R at the National Synchrotron Light Source, Rev. Sci. Instrum., 70, 2899–2904, https://doi.org/10.1063/1.1149846, 1999.

Ma, M., Liu, W., Chen, Z., Liu, Z., and Li B.: Compression and structure of brucite to 31 GPa from synchrotron X-ray diffraction and infrared spectroscopy studies, Am. Mineral., 98, 33–40, https://doi.org/10.2138/am.2013.4117, 2013.

Mackwell, S. J. and Kohlstedt, D. L.: Diffusion of hydrogen in olivine – implications for water in the mantle, J. Geophys. Res., 95, 5079–5088, 1991.

Mavrogenes, J. A. and Bodnar, R. J.: Hydrogen movement into and out of fluid inclusions in quartz: experimental evidence and geological implications, Geochim. Cosmochim. Ac., 58, 141–148, 1994.

McLaren, A. D. and Hobbs, B. E.: Transmission electron microscope investigations of some naturally deformed quartzites, in: Flow and Fracture of Rocks, edited by: Heard, H. C., Borg, I. Y., Carter, N. L., and Raleigh, C. B., Geophys. Monograph, 16, 55–66, Amer. Geophys. Union, Washington, D.C., 1972.

McLaren, A. C., Cook, R. F., Hyde, S. T., and Tobin, R. C.: The mechanisms of the formation and growth of water bubbles and associated dislocation loops in synthetic quartz, Phys. Chem. Miner., 9, 79–94, 1983.

McLaren, A. C., FitzGerald, J. D., and Gerretsen, J.: Dislocation nucleation and multiplication in synthetic quartz: relevance to water weakening, Phys. Chem. Miner., 16, 465–482, 1989.

Mitra, G., Bhattacharyya, K., and Mukul, M.: The lesser Himalayan duplex in Sikkim: implications for variations in Himalayan shortening, J. Geol. Soc. India, 75, 289–301, 2010.

Muto, J., Hirth, G., Heilbronner, R., and Tullis, J.: Plastic anisotropy and fabric evolution in sheared and recrystallized quartz single crystals, J. Geophys. Res., 116, 1–18, 2011.

Nakashima, S., Matayoshi, H., Yuko, T., Michibayashi, K., Masuda T., Kuroki, N., Yamagishi, H., Ito, Y., and Nakamura, A.: Infrared microspectroscopy analysis of water distribution in de-

formed and metamorphosed rocks, Tectonophysics, 245, 263–276, https://doi.org/10.1016/0040-1951(94)00239-6, 1995.

Ord, A. and Christie, J. M.: Flow stresses from microstructures in mylonitic quartzites of the Moine Thrust zone, Assynt area, Scotland, J. Struct. Geol., 6, 639–654, 1984.

Paterson, M. S.: The thermodynamics of water in quartz, Phys. Chem. Miner., 13, 245–255, 1986.

Paterson, M. S.: The interaction of water with quartz and its influence in dislocation flow – an overview, in: Rheology of Solids and of the Earth, edited by: Karato, S.-I. and Toriumi, M., Oxford University Press, Oxford, 107–142, 1989.

Peach, B. N., Horne, J., Gunn, W., Clough, C. T., and Hinxman, L. W.: The Geological Structure of the Northwest Highlands of Scotland, Memoir Geological Survey Great Britain, HMSO, Glasgow, 1907.

Pistorius, A. M. A. and DeGrip, W. J.: Deconvolution as a tool to remove fringes from an FT-IR spectrum, Vibrational Spectroscopy, 36, 89–95, https://doi.org/10.1016/j.vibspec.2004.04.001, 2004.

Post, A. D., Tullis, J., and Yund, R. A.: Effects of chemical environment on dislocation creep of quartzite, J. Geophys. Res., 101, 22143–22155, 1996.

Powell, R. and Holland, T.: Optimal geothermometry and geobarometry, Am. Mineral., 79, 120–133, 1994.

Seaman, S. J., Williams, M. L., Jercinovic, M. J., Koteas, G. C., and Brown, L. B.: Water in nominally anhydrous minerals: implications for partial melting and strain localization in the lower crust, Geology, 41, 1051–1054, https://doi.org/10.1130/G34435.1, 2013.

Smith, D. L. and Evans, B.: Diffusional crack healing in quartz, J. Geophys. Res., 89, 4125–4135, 1984.

Snoke, A. W., Tullis, J., and Todd, V. R.: Fault-related Rocks, A Photographic Atlas, Princeton University Press, Princeton, 617 pp., 1998.

Srivastava, P. and Mitra, G.: Thrust geometries and deep structure of the outer and lesser Himalaya, Kumaon and Garhwal (India): implications for evolution of the Himalayan fold-and-thrust belt, Tectonics, 13, 89–109, 1994.

Stahr, D. W.: Kinematic Evolution, Metamorphism and Exhumation of the Himalayan Series, Sutlej River and Zanskar Regions of NW India, PhD thesis, Virginia Tech, USA, available at: https://vtechworks.lib.vt.edu/handle/10919/23081 (last access: 26 June 2017), 2013.

Stipp, M., Stünitz, H., Heilbronner, R., and Schmid, S. M.: The eastern Tonale fault zone: a "natural laboratory" for crystal plastic deformation of quartz over a temperature range from 250 to 700 degrees C, J. Struct. Geol., 24, 1861–1884, https://doi.org/10.1016/S0191-8141(02)00035-4, 2002.

Stipp, M., Tullis, J., and Behrens, A.: Effect of water on the dislocation creep microstructure and flow stress of quartz and implications for the recrystallized grain size piezometer, J. Geophys. Res., 111, 201–220, 2006.

Stipp, M., Tullis, J., Scherwarth, M., and Behrmann, J. H.: A new perspective on paleopiezometry: Dynamically recrystallized grain size distributions indicate mechanism changes, Geology, 38, 759–762, https://doi.org/10.1130/G31162.1, 2010.

Stuart, B. H., George, B., and McIntyre, P.: Modern Infrared Spectroscopy, J. Wiley and Sons, 200 pp., 1996.

Stünitz, H., Thust, A., Heilbronner, R., Behrens, H., Kilian, R., Tarantola, A., and FitzGerald, J. D.: Water redistribution in experimentally deformed natural milky quartz single crystals – implications for H_2O-weakening processes, J. Geophys. Res., 122, 866–894, https://doi.org/10.1002/2016JB013533, 2017.

Tarantola, A., Diamond, L. W., and Stünitz, H.: Modification of fluid inclusions in quartz by deviatoric stress I: experimentally induced changes in inclusion shapes and microstructures, Contrib. Mineral. Petr., 160, 825–843, https://doi.org/10.1007/s00410-010-0509-z, 2010.

Tarantola, A., Diamond, L. W., Stünitz, H., Thust, A., and Pec, M.: Modification of fluid inclusions in quartz by deviatoric stress, III: influence of principal stresses on inclusion density and orientation, Contrib. Mineral. Petr., 164, 537–550, https://doi.org/10.1007/s00410-012-0749-1, 2012.

Thomas, S.-M., Koch-Müller, M., Reichert, P., Rhede, D., Thomas, R., Wirth, R., and Matsyuk, S.: IR calibrations for water determination in olivine, r-GeO_2, and SiO_2 polymorphs, Phys. Chem. Miner., 36, 489–509, https://doi.org/10.1007/s00269-009-0295-1, 2009.

Tobgay, T., McQuarrie, N., Long, S., Kohn, M. J., and Corrie, S. L.: The age and rate of displacement along the Main Central Thrust in the western Bhutan Himalaya, Earth Planet. Sc. Lett., 319–320, 146–158, https://doi.org/10.1016/j.epsl.2011.12.005, 2012.

Tokiwai, K. and Nakashima, S.: Integral molar absorptivities of OH in muscovite at 20 to 650°C by in-situ high-temperature IR microspectroscopy, Am. Mineral. 95, 1052–1059, 2010a.

Tokiwai, K. and Nakashima, S.: Dehydration kinetics of muscovite by in situ infrared microspectroscopy, Phys. Chem. Miner., 37, 91–101, 2010b.

Tullis, J.: Deformation of feldspars, Chap. 13, in: Feldspar Mineralogy, Second Edition, edited by P.H. Ribbe, Reviews in Mineralogy, v.2, Min. Soc. Amer., Washington DC, 297–324, 1983.

Tullis, J. and Yund, R. A.: Experimental deformation of dry Westerly granite, J. Geophys. Res., 82, 5705–5718, 1977.

Tullis, J. and Yund, R. A.: Hydrolytic weakening of experimentally deformed Westerly granite and Hale albite rock, J. Struct. Geol., 2, 439–451, 1980.

Tullis, J. and Yund, R. A.: Hydrolytic weakening of quartz aggregates: the effects of water and pressure on recovery, Geophys. Res. Lett., 16, 1343–1346, 1989.

Vannay, J. C. and Grasemann, B.: Inverted metamorphism in the High Himalaya of Himachal Pradesh (NW India): phase equilibria versus thermobarometry, Schweiz. Miner. Petrog., 78, 107–132, 1998

Weathers, M. S., Bird, J. M., Cooper, R. F., and Kohlstedt, D. L.: Differential stress determined from deformation-induced microstructures of the Moine thrust zone, J. Geophys. Res., 84, 7495–7509, 1979.

White, S.: Dislocations and bubbles in vein quartz, Nature Phys. Sci., 243, 11–14, 1973.

Woodhead, J. A., Rossman, G. R., and Thomas, A. P.: Hydrous species in zircon, Am. Mineral., 76, 1533–1546, 1991.